Chapter 6
Signals and Coils

Abstract This is a pivotal chapter in which the many background elements introduced in earlier chapters are drawn together to show how various factors affect the observed impedance of an eddy current probe coil. This chapter focuses on fundamental knowledge in eddy-current NDE, detailing the response of eddy-current probes to unflawed test-pieces of relatively simple shape. The analysis begins with the simplified case of a current sheet and half-space conductor, from which the definition of the electromagnetic skin depth emerges. Semi-analytic calculations of coil impedance are given for a coil in free space and in the vicinity of a conductor, including cases of surface and tangent coils in the vicinity of a conductive half-space and encircling or bobbin coils in the vicinity of cylindrical conductors or bore holes, respectively. The effect of important probe factors—coil dimensions, construction with or without a ferrite core, and frequency of excitation current—are discussed. Test-piece factors—conductivity, permeability, shape, and position relative to the coil—are also discussed. Sources of uncertainty in inspections due to, for example, unknown variations in the coil windings or accidental tilt of the probe during an inspection are described. The impedance-plane diagram is introduced in absolute and normalized forms.

6.1 Introduction

The purpose of this chapter is the presentation of electromagnetic theory that underlies the observed impedance of an eddy-current coil. Two important configurations are considered, from which the impedance of most eddy current probe types can be obtained. These are (i) the configuration in which a coil is oriented such that its axis is perpendicular to the surface of the test-piece (a "surface" or "normal" coil) and (ii) that in which the coil axis is ideally aligned with the axis of the test-piece, as in the case of an encircling coil or bobbin probe. In both configurations, a simple current loop is considered first and the impedance of a coil with N turns is obtained later by superposition. This chapter presents, therefore, the theoretical building blocks from which the impedance of multi-coil probes such as *differential*, *driver pick up*, *plus-point*, *array* and *hybrid* probes can be calculated. These are discussed in Chap. 8.

N. Bowler, *Eddy-Current Nondestructive Evaluation*,
Springer Series in Measurement Science and Technology,
https://doi.org/10.1007/978-1-4939-9629-2_6

The test-pieces described in this chapter are also limited to the simplest possible; the homogeneous half-space and the long rod or bore hole. A half-space is an idealized shape with a flat surface that is, in practice, sufficiently large that the coil fields are not measurably perturbed by the edges or back surface of the sample. Similarly, the long rod and bore hole are sufficiently long that end effects are not observed by the coil. Eddy-current coil response to a spherical conductor has been examined by a few authors [1–3] but the spherical test piece geometry appears to be of lower practical relevance than flat and rod-like geometries, and is not discussed explicitly in this text. More complex test-piece geometrical configurations, in particular those involving layered and truncated media, are considered in Chap. 7.

Prior to considering two-dimensional problems of circular coils interacting with various test-pieces, the one-dimensional configuration of a half-space conductor excited by a *uniform current sheet* is treated in Sect. 6.3.1. The solution for this one-dimensional configuration is important because it reveals the definition of the electromagnetic skin depth, introduced in Sect. 2.9. It is also helpful for the reader to understand the solution for the electromagnetic field in the one-dimensional configuration before moving to that for the more complex two-dimensional configurations.

In Sect. 6.3.2, two methods for calculating the magnetic field due to a circular current loop in air is described. These are interesting but not essential to the development of probe interactions with a test-piece given in Sect. 6.3.3. From the solution for the circular current loop, a solution for a multi-turn coil may be obtained in a straightforward way by superposing N such loops, as shown in Sect. 6.3.4. Building on the discussion of the multi-turn coil, the improvement in coupling to the test-piece that can be obtained by use of a ferrite core is considered in Sect. 6.3.5. The treatment of the surface coil concludes with a discussion of significant sources of noise, such as coil tilt and nonideal coil behavior due to inter-winding capacitance and finite resistance of the windings, Sect. 6.3.6. A method for correcting for nonideal behavior of an absolute probe coil is presented that is particularly useful for reducing uncertainty in benchmark experiments.

Section 6.4 provides a discussion of the impedance due to a tangent coil, whose axis is tangential to the surface of the test-piece. Tangent coils find special application as plus-point probes, in which two tangent coils are combined (Sect. 8.5). The solution by which the impedance of a tangent coil can be calculated is a limiting case of the solution for a tilted coil, Sect. 6.3.6.

In Sects. 6.5 and 6.6, the theoretical description of other commonly employed configurations, in which the coil axis is parallel to the axis of the test-piece, are presented. Again, from the solution for the circular current loop, that for a multi-turn coil may be obtained by superposition. The configuration is relevant to test scenarios such as a coil encircling a cylindrical rod and a bobbin coil inspecting the interior of a bore hole or tube. In these systems of cylindrical symmetry, two sources of geometrical uncertainty exist; coil tilt and *wobble*. As in the case of the surface coil, tilt occurs when the coil axis tilts through a finite angle with respect to the axis of the test-piece—here either a rod or a bore hole. Wobble occurs when the

coil axis is laterally displaced from the axis of the test-piece. Both of these effects are important to understand because they lead to signal noise that might obscure a genuine indication from a defect or other feature.

6.2 Coil Impedance

The impedance of an eddy current coil, Z, defined in Sect. 4.9, is the quantity measured in an EC NDE inspection. In Chaps. 2 and 4, we have discussed the fact that the impedance of an eddy current coil is determined by the value of its resistance, capacitance, and inductance. For the purposes of EC NDE, the inductance is the most important of these since it is the circuit quantity that represents the presence of the magnetic field in the coil, and in EC NDE it is this magnetic field that couples with the part under test and induces eddy currents in it. An *ideal* eddy-current coil would be a pure inductor with inductance L and impedance

$$Z_{\text{ideal}} = j\omega L. \tag{6.1}$$

A real coil, however, exhibits resistance R and capacitance C in addition to inductance. Resistance of a real coil arises due to the finite resistivity of the wire used in the coil windings and cables. Coil capacitance makes a significant contribution to the probe impedance when the frequency of operation of the probe is increased to a value that depends upon the particular construction of the coil, i.e., its number of turns and geometrical parameters. The source of C is the close proximity (to each other) of the coil windings and connecting wires. Thus, while L is the quantity of real interest in EC NDE, R and C cannot be eliminated in a real probe and contribute to its impedance.

6.2.1 Isolated Coil Impedance, Z_0

The impedance of an *isolated* coil, Z_0, is the value of impedance of a coil when it is remote from the test-piece or any other metal. It is also referred to as the impedance of the coil *in air*. In general, $Z_0 = R_0 + jX_0$, where R_0 and X_0 are the resistance and reactance of the isolated coil, (4.27). The value of Z_0 is primarily determined by the number of turns on the coil, its shape and dimensions.

If R_0 and stray capacitances associated with the probe are considered to be negligible, which is often approximately true for frequencies well below the resonant frequency of the coil, then $Z_0 \approx j\omega L_0 = jX_0$ where L_0 is the DC inductance of the coil. This is an "ideal" case for EC NDE because the useful interaction between an EC probe and a test-piece is mediated by inductance, as mentioned above.

Other measurements of coil impedance, when the coil field interacts with a test-piece, are often normalized with respect to $\text{Im}\{Z_0\} = X_0$.

6.2.2 *Coil Impedance in the presence of a Conductor, Z, and the Impedance-Plane Plot*

When a coil is moved from "air" (its isolated position) to the surface of a conductor, its impedance changes from Z_0 to Z. The precise value of Z depends on geometrical effects such as the proximity and orientation of the coil with respect to the test-piece, and the test-piece parameters conductivity and permeability.

In a typical EC inspection, impedance data are displayed in the form of a two-dimensional plot in which the real and imaginary parts of the coil impedance are displayed on orthogonal axes. An inspector observes the locus of points traced on the instrument display as the probe is moved in relation to the test-piece.

The impedance-plane plot sketched in Fig. 6.1 shows several possibilities for the change in coil impedance $Z = R + jX$ as the coil is moved from air to either a non-ferromagnetic or a ferromagnetic metal test-piece. These curves may be explained qualitatively as follows. When a probe is moved from isolation (air) to the surface of a non-ferromagnetic metal test-piece, its resistance increases whereas its reactance decreases, as indicated by the symbol Z_{n-f} in Fig. 6.1. The effective coil resistance increases in response to the fact that eddy currents are now flowing in the nearby test-piece, extracting energy from the probe and effectively increasing its resistance. The coil reactance decreases, on the other hand, due to the fact that the eddy currents induced in the test-piece circulate in a direction opposite to the direction of current flow in the coil, by Lenz's Law. Consequently, the magnetic induction field associated with the coil current is effectively reduced by the opposing magnetic induction field associated with the eddy currents, resulting in an overall reduction of the inductance of the coil. Example lift-off curves that are generated as an isolated coil is moved to the surface of a slab of bronze, at three different frequencies, are shown as broken lines in Fig. 6.2. Similar curves could be plotted as the probe moves from the air

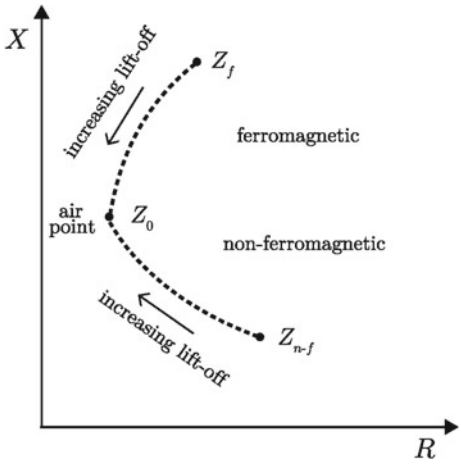

Fig. 6.1 Possible changes in coil impedance as the coil is moved from the air point, where it is isolated from any conductive material and exhibits impedance Z_0, to ferromagnetic and non-ferromagnetic conductors where its impedance becomes Z_f and Z_{n-f}, respectively

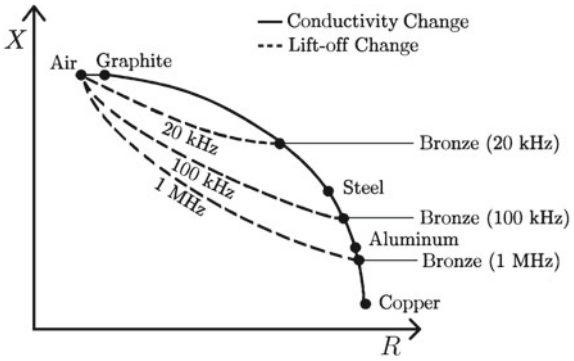

Fig. 6.2 Impedance-plane diagram for a surface coil, showing the air point at which the coil is remote from any test-piece, and impedance values (•) obtained when the coil is in contact with the surface of various metals. The coil operates at 20 kHz except where indicated. Broken lines (- - -) represent the impedance as a function of lift-off from the surface of a bronze test-piece, at three different frequencies

point to the surface of other types of metal, some of which are indicated in the figure. For any particular coil, the path of the lift-off curve that is observed depends on the test-piece conductivity and permeability and on the frequency of the inspection. Note that one practical use of lift-off curves are for determining the thickness of nonconductive, non-ferromagnetic, surface coatings on a metal substrate. Examples of such coatings are paints and lacquers.

Considering now the case of a probe moving from isolation to the surface of a ferromagnetic metal test-piece, indicated by point Z_f in Fig. 6.1, the increase in coil resistance is explained in the same way as for the case of the non-ferromagnetic test-piece, discussed above. The observed *increase* in inductance is, however, opposite in sign to the change observed in the case of non-ferromagnetic test material. This observation is explained by the fact that the strength of the magnetic induction field associated with the coil itself now increases when the coil nears the test-piece, due to the fact that the coil field is strengthened by the ferromagnetism of the test-piece (Chap. 3). The magnetic induction field associated with the induced eddy currents still opposes that of the coil, but the increased strength of the coil field dominates, resulting in an overall increase in the inductance of the coil.

Quite commonly, especially in the case of *calculated* impedance, values of resistance and reactance are plotted that are normalized with respect to the reactance of the isolated coil. In other words, the horizontal and vertical axes display the real and imaginary parts, respectively, of

$$\frac{Z}{X_0} = \frac{R - R_0}{X_0} + j\frac{X}{X_0}. \tag{6.2}$$

It is useful to be familiar with this form of data presentation because in several aspects it appears different to the impedance-plane plots of Figs. 6.1 and 6.2. Notice

also that the real part of the isolated coil impedance, R_0, is subtracted from R prior to normalization with respect to X_0. This means that, as the lift-off increases, the curves tend toward the value of the probe impedance in air which is indicated by $Z_0/X_0 = 0 + j1$, Fig. 6.3. This point is the air point, on the normalized Z-plane plot. If we were to extrapolate the solid lines in Fig. 6.3 to higher frequencies, they

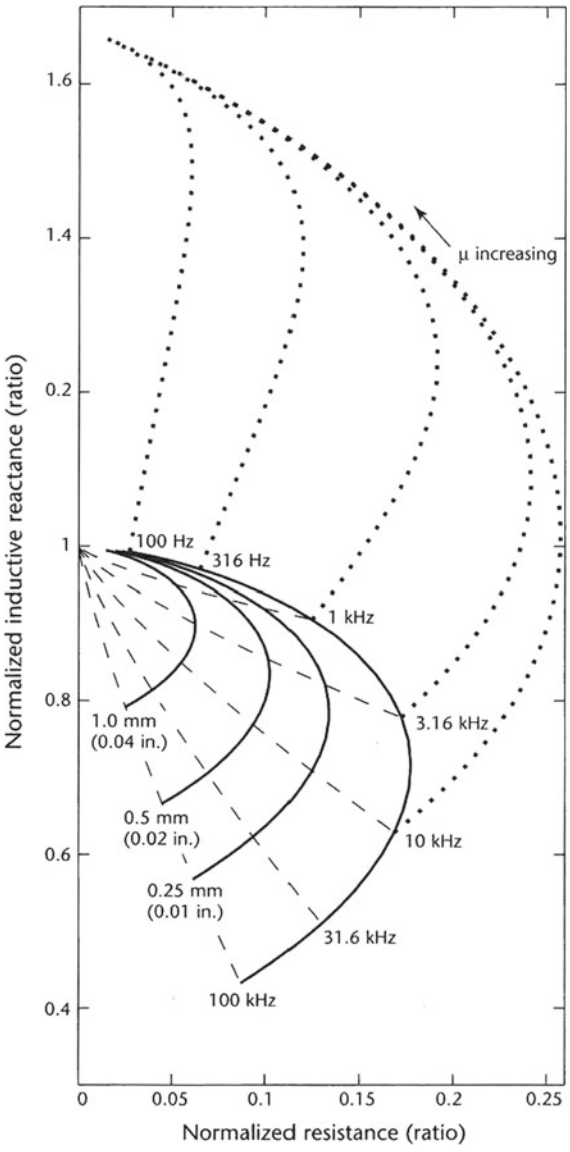

Fig. 6.3 Normalized impedance-plane diagram for a surface coil. Normalized inductive reactance $= X/X_0$ and normalized resistance $= (R - R_0)/X_0$. Solid lines (——) represent the complex impedance of the probe as a function of frequency. Broken lines (- - -) represent the impedance as a function of lift-off. Dotted lines (· · ·) indicate the influence of permeability of the specimen on the probe impedance. The point given by the coordinates (0, 1) is the air point. For the particular impedance values shown in this plot, the probe parameters are $r_i = 2$ mm, $r_o = 4$ mm, $l = 1$ mm and $N = 800$, and the test-piece is a half-space ($T \to \infty$) with $\sigma = 35.4$ MS/m and $\mu_r = 1$. Reprinted with permission from the NDT Handbook: Electromagnetic Testing. Copyright ©2004, ASNT, Columbus, Ohio [4]

would approach the vertical axis at different points. In fact, in the high- frequency regime, the curves can be described asymptotically by the relation

$$\frac{X}{X_0} = \frac{R - R_0}{X_0} + c, \tag{6.3}$$

which is the equation of a straight line with unit slope and intercept c on the axis of X/X_0. The value of c is given by the ratio X/X_0 in the asymptotic (high-frequency) limit and provides an indication of the strength of coupling between the probe coil and the test-piece. The larger the value of $|c|$, the stronger the coupling between the probe and the test-piece.

6.2.3 Coil Impedance Change Due to a Flaw, ΔZ

When a coil is moved from a position on an unflawed region of a test-piece, to a region where the presence of a defect perturbs the induced eddy currents, there is a change in the impedance of the coil; ΔZ. This impedance change is defined as

$$\Delta Z = Z - Z_{\text{flaw}}, \tag{6.4}$$

where Z is the impedance when the coil is on the test-piece but far from a flaw, and Z_{flaw} is the impedance of the coil in the vicinity of a flaw.

An example of the magnitude of impedance change obtained as a coil scans over a slot in a metal plate is shown in Fig. 6.4 [5].

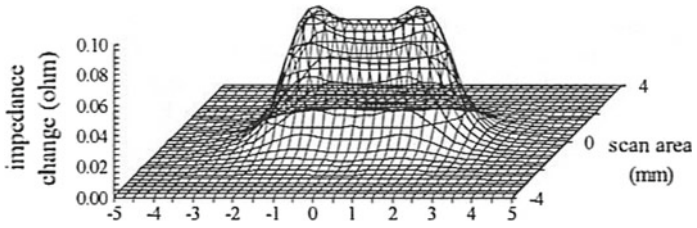

Fig. 6.4 Magnitude of the impedance change, $|\Delta Z|$, obtained by two-dimensional scanning of an eddy current probe over a through-slot in a metal plate. The physical and geometrical parameters of the probe, plate, and defect are given in Table 6.1. Reprinted from Badics, Z., Kojima, S., Matsumoto, Y., Aoki, K., Nakayasu, F.: Comparison of different "Matrix Multisensor" ECT probe designs by three-dimensional electromagnetic modeling. In: Collins, R., Dover, W.D., Bowler, J.R., Miya, K. (eds.) Nondestructive Testing of Materials. Studies in Applied Electromagnetics and Mechanics, vol. 8, pp. 13–20. IOS Press, Amsterdam (1995), p. 18, Fig. 2 [5], with permission from IOS Press

Table 6.1 Probe, plate, and defect parameters for the impedance change plotted in Fig. 6.4 [5]. The probe is formed from two square, printed-circuit coils—one driver and one pick up—separated by a 0.2-mm-thick substrate. The pick up coil contacts the test-piece. The test-piece is nuclear power plant steam generator tube material, of type and thickness not specified in the original paper. The flaw is an electro discharge machined (EDM) notch

Coil parameters		Value	Flaw parameters		Value
d_o	Outer dimension (mm)	2.00	l	Length (mm)	3.0
d_i	Inner dimension (mm)	0.72	w	Width (mm)	0.2
s	Coil stand-off (mm)	0.0	d	Depth	Through-wall
h	Probe lift-off (mm)	0.1			
n	Number of turns	40			
f	Inspection frequency (kHz)	200			

Many more examples, and techniques for calculating ΔZ due to various types of defect, are given in Chap. 9. The primary objective of the present chapter is to describe how Z is computed for various probe types when the probe interacts with an unflawed specimen.

6.3 Surface Coil

A surface coil is defined as one whose axis is parallel with the direction of the unit vector normal to the surface being inspected. An air-cored surface probe is shown schematically in Fig. 1.9. Surface coils can also be used to evaluate test-pieces with more complicated geometry, such as the interior of a borehole or tube, as shown in Fig. 6.5. Note that the axis of the coil in this configuration is still perpendicular to the surface under test. Many different designs of surface probes exist, for different inspection needs. Surface probes often operate in *absolute mode*, Sect. 8.2, meaning that the signal obtained in a measurement is simply the value of the coil impedance itself. *Differential* and *driver pick up* surface probes are also common, described in Sects. 8.3 and 8.4, respectively.

A normalized impedance-plane diagram obtained for a surface coil located above a conductive half-space is shown in Fig. 6.3. In practice, a small part of the impedance-plane plot is displayed by an oscilloscope (or *eddyscope*). It is common practice, in an eddy-current inspection, to "rotate" the display so that the change in Z due to lift-off variation appears horizontally on the eddyscope display. Then, indications due to flaws and other features can be easily distinguished from noise due to lift-off variations or tilt angle of the probe, as it scans the test-piece.

Fig. 6.5 Sectional view of the interior of a bore hole or tube inspected by a rotary surface coil. Note that the coil axis is parallel with the direction of the unit vector normal to the surface being inspected, here the $\hat{\rho}$-direction. In practice, the coil would be mounted in a rotary probe (not shown here) in order to inspect the entire interior surface of the borehole via a helical path

Considering the impedance-plane plot of Fig. 6.3, the solid curves represent the complex impedance of the probe as a function of frequency. Each solid curve is for a different value of the probe lift-off, as marked. The broken lines show the impedance as a function of lift-off from the conductor surface. In Fig. 6.3 the coupling (see discussion in Sect. 6.2.2) is clearly the strongest for the case in which the coil is nearest to the test-piece (the lift-off is the smallest) - a result that happily agrees with common sense! Impedance-plane plots such as this one can be computed or obtained by experimentation for various coil and test-piece configurations. Looking ahead to two other examples; it is shown in Fig. 6.14 that coupling increases when a coil is filled with a ferrite core and, for a coil encircling a rod, Fig. 6.23, coupling increases as the space between the coil and rod decreases, i.e., as the fill factor increases.

In Fig. 6.2, as well as the effect of lift-off discussed earlier, the effect on the Z-plane plot of changes in conductivity of the test-piece is shown. Note, the impedance change due to a change in probe lift-off, and the impedance change due to a change in conductivity, are more clearly distinguished at the higher frequencies shown because there is a greater angle between their effects in the Z-plane than at lower frequencies. At lower frequencies (such as 100 Hz in Fig. 6.3) it is very difficult to differentiate between lift-off and conductivity changes in Z. This kind of observation shows how impedance-plane plots can be used to guide the choice of inspection parameters, such as the frequency of coil operation, to optimize the sensitivity of an inspection for its particular purpose.

6.3.1 *Excitation of a Half-Space Conductor by a Uniform Current Sheet*

Having examined Maxwell's equations and the interface conditions on the electromagnetic field in Chap. 5, we are in a position to solve a problem—our first—in which an exciting current flowing *near to* a metal test-piece induces currents *in* the metal. The geometry that we shall consider is the simplest one possible; a uniform current sheet parallel to an infinitely deep (so-called *half-space*) conductor, as shown in Fig. 2.5. In this case the properties of the half-space conductor are assumed linear, isotropic and homogeneous, i.e., σ and μ_r are everywhere scalar and constant. This is a one-dimensional problem because the fields vary only in the direction perpendicular to the conductor surface, the z-direction. The solution of Maxwell's equations for this system will reveal the definition and meaning of the electromagnetic penetration depth introduced in Sect. 2.9. This problem is also a useful introduction to the more complex, two-dimensional, problem of the excitation of a half-space conductor by a circular coil, which will be considered in Sects. 6.3.3 and 6.3.4.

This is an artificial problem in the sense that no real coil is an infinite current sheet, but the solution obtained here may be applicable to real systems under certain circumstances. For example, parallel windings of a coil around a wide, thick plate give rise to an approximately uniform current sheet in regions sufficiently far from the edges. Second, a surface coil wound on a cylindrical former produces a current density that appears uniform on a scale somewhat less than the coil diameter, as shown in Fig. 6.6. Further, some coils are purposely designed to induce an eddy current density that is approximately uniform over a prescribed region of the surface of a test-piece [6].

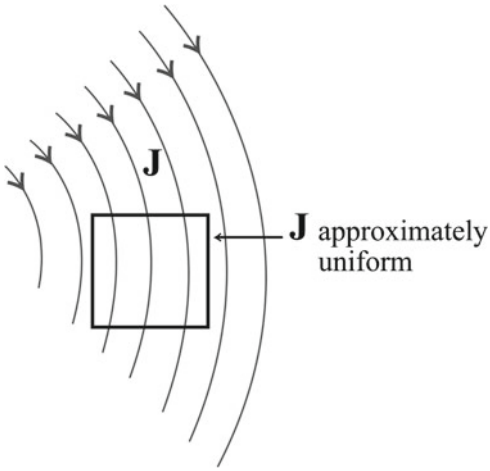

Fig. 6.6 A large-diameter coil shows a region of approximately uniform current density **J** on a scale somewhat smaller than the coil diameter

Governing Equation

We will begin by manipulating Maxwell's equations to obtain an equation which *governs* the behavior of the electric field in the system shown in Fig. 2.5. First, write down the phasor forms of Faraday's Law and the quasi-static Maxwell–Ampère Law as follows:

$$\nabla \times \mathbf{E} = -j\omega\mathbf{B}, \tag{6.5}$$

$$\nabla \times \mathbf{H} = \mathbf{J}. \tag{6.6}$$

Now write $\mathbf{J}$ as a sum of the current density in the source coil, $\mathbf{J}_s$, and the eddy-current density induced in the test-piece, $\mathbf{J}_{ec}$. Then,

$$\nabla \times \mathbf{H} = \mathbf{J}_s + \mathbf{J}_{ec}. \tag{6.7}$$

Take the curl of Faraday's Law, (6.5), substitute for $\mathbf{B}$ by means of constitutive relation (2.25) for isotropic permeability and then use (6.7) to obtain

$$\nabla \times \nabla \times \mathbf{E} = -j\omega\mu \left(\mathbf{J}_s + \mathbf{J}_{ec}\right). \tag{6.8}$$

Make the substitution $\mathbf{J}_{ec} = \sigma\mathbf{E}$, (2.15), and employ vector identity (10.46) to obtain

$$\nabla\nabla \cdot \mathbf{E} - \nabla^2\mathbf{E} = -j\omega\mu \left(\mathbf{J}_s + \sigma\mathbf{E}\right). \tag{6.9}$$

In the case of zero free volume charge, $\rho_v = 0$ and $\nabla \cdot \mathbf{D} = \epsilon\nabla \cdot \mathbf{E} = 0$. That is, $\nabla \cdot \mathbf{E} = 0$ and

$$\left(\nabla^2 - j\omega\mu\sigma\right)\mathbf{E} = j\omega\mu\mathbf{J}_s. \tag{6.10}$$

This is the governing equation for the electric field. In actual fact it is valid for any geometrical configuration of current source $\mathbf{J}_s$ and conductive test-piece, not only for the one-dimensional system that we are considering at the moment, Fig. 2.5. By similar steps it can be shown that the magnetic field obeys the governing equation

$$\left(\nabla^2 - j\omega\mu\sigma\right)\mathbf{H} = -\nabla \times \mathbf{J}_s. \tag{6.11}$$

(The derivation of this equation is the subject of Exercise 1 at the end of this chapter.)

Focusing now on the one-dimensional system shown in Fig. 2.5, in which a uniform current sheet in the plane $z = h$ excites a half-space conductor that occupies $z < 0$, identify

$$\mathbf{J}_s = \mathcal{I}\delta(z - h)\hat{x} \tag{6.12}$$

where $\mathcal{I}$ is the phasor amplitude of the alternating current being carried in the sheet at $z = h$. The delta function, $\delta(x)$, can be viewed as the derivative of the Heaviside step function $H(x)$. The delta function displays the following fundamental properties:

$$\int_{-\infty}^{\infty} f(x)\delta(x - x_0)dx = f(x_0), \tag{6.13}$$

$$\int_{x_0-\epsilon}^{x_0+\epsilon} f(x)\delta(x - x_0)dx = f(x_0), \qquad \epsilon > 0, \tag{6.14}$$

$$\delta(x - x_0) = 0, \qquad x \neq x_0. \tag{6.15}$$

In the context of (6.12), the delta function indicates that the current is confined to an infinitesimally thin sheet at $z = h$. Noting that the only variation in the fields is as a function of z, and that $\mathbf{E} = E_x\hat{x}$ must be x-directed as is the source $\mathbf{J}_s$, allows us to write a simplified form of (6.10) as follows:

$$\left(\frac{d^2}{dz^2} - k^2\right) E_x(z) = j\omega\mu\mathcal{I}\delta(z - h), \tag{6.16}$$

where we have identified

$$k^2 = j\omega\mu\sigma \tag{6.17}$$

and k will turn out to be a complex wavenumber which controls the propagation and absorption, or loss, of the electromagnetic field in the test-piece. By convention, we require that k is obtained by taking the root of k^2 that has positive real part. That is,

$$k = \sqrt{\frac{\omega\mu\sigma}{2}}(1 + j). \tag{6.18}$$

Equation (6.16) is a simple one-dimensional differential equation. Solve it by writing down separate equations for the current source region, $z > 0$, and the conductor region, $z < 0$. These equations recognize the current source at $z = h$, located in a region that is otherwise nonconductive (air), and the conductive nature of the test-piece in the negative half-space.

$$\frac{d^2E_x(z)}{dz^2} = j\omega\mu\mathcal{I}\delta(z - h), \quad z > 0, \tag{6.19}$$

$$\left(\frac{d^2}{dz^2} - k^2\right) E_x(z) = 0, \quad z < 0. \tag{6.20}$$

Solution

In the conductor, the general solution for $E_x(z)$ is of the form

$$E_x(z) = E_0[e^{jkz} + Ce^{-jkz}] \tag{6.21}$$

where E_0 is the magnitude of the electric field at the conductor surface. Physically, the field cannot grow as distance from the source current increases (as $z \to -\infty$), so $C = 0$ and

$$E_x(z) = E_0e^{jkz}. \tag{6.22}$$

This solution reveals that the eddy-current density in this setup decays exponentially as a function of depth into the conductor. Substituting for k from (6.18) into (6.22) gives

$$E_x(z) = E_0 e^{(1+j)z/\delta} \tag{6.23}$$

where the electromagnetic skin depth, or penetration depth, is defined as

$$\delta = \sqrt{\frac{2}{\omega\mu\sigma}}. \tag{6.24}$$

This quantity was introduced in Sect. 2.9. The current density in the metal obeys the same form as the electric field since they are related linearly by the conductivity of the conductor via Ohm's law (2.15), so

$$J_x(z) = J_0 e^{(1+j)z/\delta}, \tag{6.25}$$

where J_0 is the magnitude of the current density at the conductor surface. It was noted in Sect. 2.9, and shown in Fig. 2.6, that the amplitude of the current density declines exponentially as a function of distance into the conductor. From (6.25), we see now that there is a linear phase change in J_x as a function of z. For example, at $z = -\delta$, $\arg(J_x)$ is -1 radian so the phase of J_x at the surface is 1 radian in advance of that at $z = -\delta$.

6.3.2 *Circular Current Loop in Air*

Analysis of the electromagnetic behavior of a circular current loop can form the basis of treatment of a finite eddy current "pancake" coil with multiple windings. In this section, two derivations of the field of magnetic induction, **B**, due to a circular current loop in air are given. These are interesting, and one method (that uses the Biot–Savart Law) can be applied to solve other similar problems. Both methods rely, however, on symmetry about the plane of the loop and consequently are not useful for deriving an expression for the electric field due to an eddy-current surface coil interacting with a test-piece. This more important configuration is treated in Sect. 6.3.3.

Biot–Savart Law

The Biot–Savart Law relates magnetic induction field **B** to the electric current which is the source of **B**. For current I flowing in a conductor as shown in Fig. 6.7,

$$d\mathbf{B} = \frac{\mu_0 I}{4\pi} \frac{d\mathbf{l} \times \hat{\imath}_r}{r^2} \tag{6.26}$$

in differential form, or,

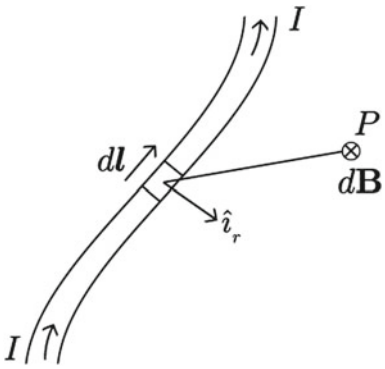

Fig. 6.7 Schematic diagram showing one configuration for application of the Biot–Savart Law

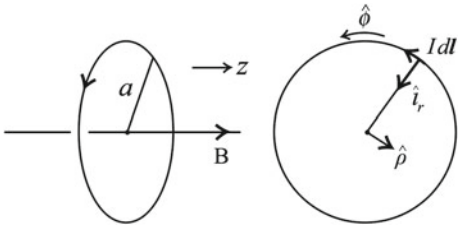

Fig. 6.8 Schematic diagram showing configuration for derivation of **B** at the center of a current loop, using the Biot–Savart Law

$$\mathbf{B} = \frac{\mu_0 I}{4\pi} \int \frac{d\mathbf{l} \times \hat{i}_r}{r^2}. \tag{6.27}$$

In these equations, $I d\mathbf{l}$ represents an infinitesimal current element. Each element makes a contribution $d\mathbf{B}$ to $\mathbf{B}$ at a field point P located at distance r from the current element. The element of magnetic induction field $d\mathbf{B}$ is directed perpendicular to the directions of both the current element $I d\mathbf{l}$ and that of the radius vector $\hat{i}_r$, in accordance with the vector product between them. In order to express $\mathbf{B}$ due to a wire made up of many elements $d\mathbf{l}$, the contribution of the individual elements is summed, which amounts to integrating over the length of the current wire, as expressed in (6.27). The direction of the magnetic induction field follows the right-hand rule and arises from the vector product contained within (6.26) and (6.27).

The current elements that feature in the Biot–Savart Law are assumed to be constrained, as if the current was flowing in a wire. This means that the Biot–Savart Law does not lend itself to calculation of the secondary magnetic induction field associated with the eddy currents themselves, $\mathbf{B}_{ec}$, because the eddy currents are distributed and best represented by a spatially varying current density $\mathbf{J}_{ec}$. To express $\mathbf{B}_{ec}$ for a particular test geometry, which may also include a defect of some kind, it is necessary to solve governing equations of the electromagnetic field for the particular setup, which can be derived from Maxwell's equations.

Example: Derivation of B at the center of a current loop, using the Biot–Savart Law Consider a circular current loop radius a carrying current I, as shown in Fig. 6.8.

In a cylindrical system with coordinates (ρ, ϕ, z) and axis coinciding with the axis of the current loop, $\hat{\imath}_r \equiv -\hat{\rho}$ and $d\mathbf{l} \equiv \rho\, d\phi\, \hat{\phi}$. Consequently,

$$\begin{aligned}\mathbf{B} &= \frac{\mu_0 I}{4\pi} \int_0^{2\pi} \frac{\rho\, d\phi\, \hat{\phi} \times (-\hat{\rho})}{\rho^2} \\ &= \hat{z} \frac{\mu_0 I}{4\pi} \int_0^{2\pi} d\phi \\ &= \hat{z} \frac{\mu_0 I}{2a}. \end{aligned} \tag{6.28}$$

This result may be generalized readily to obtain an expression for **B** along the entire axis of the wire—see Exercise 2 at the end of this chapter. The limitations of the Biot–Savart Law may quickly be seen by considering a field point off the axis, however. In this case, the distance between the current element and field point, r, varies as contributions from the various current elements around the loop are considered and we observe that the Biot–Savart Law is useful for obtaining simple analytical expressions for **B** only in a limited set of geometrical configurations. It may be used to evaluate **B** numerically in more complex configurations, however.

Magnetic Vector Potential

In [7], there is a beautiful derivation of the analytical expression for **B** at all points in space due to a current loop in free space. The derivation is reproduced in this section but, first, the theoretical reasoning that defines the magnetic vector potential **A** according to the Coulomb gauge is presented. The potential **A** was introduced in Sect. 5.5.1. It is employed in the derivation given in [7] and also in the seminal works of C. V. Dodd and W. E. Deeds that consider the response of a pancake coil near a conductive test-piece [8, 9], to be presented in Sects. 6.5 and 6.6 of this text. Despite the fact that the original solutions were written in terms of A_ϕ, the solutions are given in Sects. 6.5 and 6.6 in terms of E_ϕ directly, via (6.44).

In the absence of magnetic materials, the Maxwell–Ampère Law may be written

$$\nabla \times \mathbf{B} = \mu_0 \mathbf{J} \tag{6.29}$$

and, as usual,

$$\nabla \cdot \mathbf{B} = 0. \tag{6.30}$$

These governing equations will be solved by introducing the magnetic vector potential **A** such that

$$\nabla^2 \mathbf{A} = -\mu_0 \mathbf{J} \tag{6.31}$$

with the condition that **A** is *regular* at ∞. (A function is said to be regular in a particular region if it is analytic and single-valued in that region. A complex function is analytic in a particular region if it is differentiable at every point in that region.)

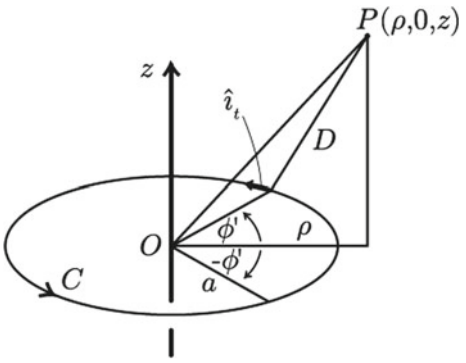

Fig. 6.9 Configuration used in solving for the vector potential, **A**, due to a current loop following path C

Equation (6.31) is obtained by choosing the gauge condition $\nabla \cdot \mathbf{A} = 0$, which is known as the Coulomb gauge. Equation (6.31) has solution

$$\mathbf{A}(\mathbf{r}) = \frac{\mu_0}{4\pi} \int_{\text{all space}} \frac{\mathbf{J}(\mathbf{r}')}{|\mathbf{r} - \mathbf{r}'|} dV' \tag{6.32}$$

where the prime denotes the source coordinates. Next, replace the volume integral in (6.32) with a line integral over path C as follows.

$$\mathbf{A}(\mathbf{r}) = \frac{\mu_0 I}{4\pi} \int_C \frac{d\mathbf{l}'}{|\mathbf{r} - \mathbf{r}'|} \tag{6.33}$$

If C is the loop shown in Fig. 6.9, then $d\mathbf{l}' = a\,\hat{i}_t\,d\phi' = a\,\hat{\phi}\,d\phi'$, $D^2 = |\mathbf{r} - \mathbf{r}'|^2 = a^2 + \rho^2 + z^2 - 2a\rho\cos\phi'$ and, noting that **A** is independent of ϕ,

$$\mathbf{A}(\rho, z) = \hat{\phi}\frac{\mu_0 I}{4\pi} \int_C \frac{a}{D} d\phi'. \tag{6.34}$$

Symmetry shows that the contributions of two current elements positioned symmetrically with respect to $\phi = 0$ sum to give a vector whose direction is perpendicular to the plane, since the parallel components sum to zero. The same argument applies for all planes of $\phi =$ constant which means that (i) **A** is $\hat{\phi}$-directed (as already written in the previous equation) and (ii) the magnitude of **A**, denoted A, can be obtained by projecting components from two symmetric elements onto their plane of symmetry and integrating around half the loop C:

$$A_\phi(\rho, z) = \frac{\mu_0 I}{4\pi} \int_0^\pi \frac{2a\cos\phi'}{(a^2 + \rho^2 + z^2 - 2a\rho\cos\phi')^{1/2}} d\phi'. \tag{6.35}$$

This expression may be rewritten by introducing the elliptic modulus, k, defined below. Note, the elliptic modulus is not the same as the complex wavenumber introduced in (6.16)–(6.18) although it shares the same symbol.

$$k = \left[\frac{4a\rho}{(a+\rho)^2 + z^2}\right]^{1/2}$$

giving

$$A_\phi(\rho, z) = \frac{\mu_0 I}{k\pi}\left(\frac{a}{\rho}\right)^{1/2}\left[\left(1 - \frac{k^2}{2}\right)K - E\right]. \tag{6.36}$$

In (6.36), K and E are complete elliptic integrals of the first and second kinds defined by

$$K(k) = \int_0^{\pi/2} \frac{d\theta}{(1 - k^2 \sin^2\theta)^{1/2}} \tag{6.37}$$

$$E(k) = \int_0^{\pi/2} (1 - k^2 \sin^2\theta)^{1/2} d\theta. \tag{6.38}$$

Magnetic Induction

In [7, Sect. 6.1], it is shown that $\mathbf{B} = \nabla \times \mathbf{A}$, as given in (5.18), making it possible to calculate $\mathbf{B}$ via the auxiliary quantity $\mathbf{A}$. Taking the curl of (6.32) gives

$$\mathbf{B}(\mathbf{r}) = \frac{\mu_0}{4\pi}\int_{\text{all space}} \nabla \times \frac{\mathbf{J}(\mathbf{r}')}{|\mathbf{r} - \mathbf{r}'|}\, dV' \tag{6.39}$$

$$= \frac{\mu_0}{4\pi}\int_{\text{all space}} \left[\nabla \frac{1}{|\mathbf{r} - \mathbf{r}'|} \times \mathbf{J}(\mathbf{r}')\right] dV' \tag{6.40}$$

$$= -\frac{\mu_0}{4\pi}\int_{\text{all space}} \frac{(\mathbf{r} - \mathbf{r}') \times \mathbf{J}(\mathbf{r}')}{|\mathbf{r} - \mathbf{r}'|^3}\, dV' \tag{6.41}$$

where identity (10.45), Sect. 10.3, has been used and it has been observed that the curl of $|\mathbf{r} - \mathbf{r}'|^{-1}$ is identically zero. Equation (6.41), unlike the Biot–Savart Law, is a mathematical expression of Ampère's Law.

From this expression, the components of the magnetic induction field $\mathbf{B}$ can be calculated and are given as follows—see Exercise 4 at the end of this chapter:

$$B_r(\rho, z) = \frac{\mu_0 I}{2\pi}\frac{z}{\rho[(a+\rho)^2 + z^2]^{1/2}}\left[-K + \frac{a^2 + \rho^2 + z^2}{(a-\rho)^2 + z^2}E\right] \tag{6.42}$$

$$B_z(\rho, z) = \frac{\mu_0 I}{2\pi}\frac{1}{[(a+\rho)^2 + z^2]^{1/2}}\left[+K + \frac{a^2 - \rho^2 - z^2}{(a-\rho)^2 + z^2}E\right] \tag{6.43}$$

Electric Field

Finally, for a time-harmonic current excitation of the form $e^{j\omega t}$, Faraday's Law may be written as in (6.5). Then, using (5.18), it is found that

$$\mathbf{E} = -j\omega\mathbf{A}. \tag{6.44}$$

Equation (6.44) indicates a simple linear relationship between the magnetic vector potential and the electric field. From this relationship we see that, for a time-harmonic excitation, the solution for the electromagnetic field due to a circular current loop presented in this section could be equally well formulated in terms of **E**.

6.3.3 Circular Current Loop above a Half-Space Conductor

In their seminal work published in 1968, C. V. Dodd and W. E. Deeds derived an analytical solution for the impedance of a surface coil located above a planar conductor with its axis perpendicular to the conductor surface [8]. Initially, a current loop with infinitesimal cross section was considered. Ultimately, a semi-analytical expression for the impedance of a coil with finite cross section was obtained, for the coil located above a two-layer planar conductor, and for a similar coil encircling a two-layer conductive rod. Later, a similar solution was published for a coil coaxial with an arbitrary number of cylindrical conductors [9]. The latter solution can represent the response of a coil encircling a layered rod, or within a borehole, or a combination of these.

These different cases are treated in this text as follows. In this section the case of the current loop and half-space conductor is considered. In Sects. 6.3.4, 6.5.1 and 6.5.2, the coil and half-space conductor, the current loop and cylindrical conductor, and the coil and cylindrical conductor are considered. Layered conductors are treated in Chap. 7.

Dodd and Deeds' original solution was formulated in terms of **A** although relation (6.44) prompts formulation in terms of **E**, which is what we will do here. Once the solution for **E** has been obtained, the voltage in the coil can be obtained by integrating the electric field around the coil windings. The impedance can then be obtained by means of relation (4.25).

Governing Equation for E

Consider a filamentary circular current loop, radius a, height h above a planar conductor with conductivity σ, Fig. 6.10. The conductor in this case is non-ferromagnetic. As in Sect. 6.3.2, the system is axially symmetric so that the current density in the loop may be expressed

$$\mathbf{J}_s = J_{s\phi}\hat{\phi} \tag{6.45}$$

which immediately implies that

$$\mathbf{E} = E_\phi \hat{\phi}. \tag{6.46}$$

In this derivation it is also assumed that the conductor is linear, isotropic and homogeneous such that constitutive relations (2.25) and (2.33) hold. The consequence of this assumption in the case of a ferromagnetic conductor is that the relations to be developed are strictly accurate only for low applied **H**, due to the assumption of a linear relationship between **B** and **H**. The restriction of low applied **H** is not

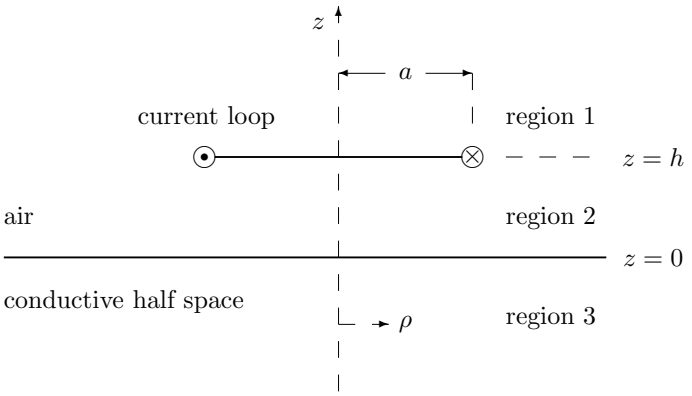

Fig. 6.10 Cross section through the axis of a circular, infinitesimal current loop, positioned horizontally above a metal half-space

required in the case of non-ferromagnetic conductors. A more detailed discussion of the nonlinear behavior of ferromagnetic materials is given in Chap. 3.

As noted above, the solution can be formulated in terms of the electric field. In fact, since the system is cylindrically symmetric, only the $\hat{\phi}$-component of the field is needed, as noted in (6.46). From Maxwell's equations, the governing equation for $\mathbf{E}$ is as given in (6.10) but here $\mathbf{E}$ has only an azimuthal component and

$$\nabla^2 \mathbf{E} = \left(\nabla^2 - \frac{1}{\rho^2}\right) E_\phi \hat{\phi}. \tag{6.47}$$

To obtain (6.47), (10.29) has been applied, noting that derivatives with respect to ϕ vanish due to axial symmetry. Expanding $\nabla^2 E_\phi$ by use of (10.28) and inserting into (6.10) gives

$$\left(\frac{\partial^2}{\partial \rho^2} + \frac{1}{\rho}\frac{\partial}{\partial \rho} - \frac{1}{\rho^2} + \frac{\partial^2}{\partial z^2} - k^2\right) E_\phi = j\omega\mu J_{s\phi} \tag{6.48}$$

where $k^2 = j\omega\mu\sigma$. For phasor current $\mathcal{I}$ flowing in an infinitesimal coil that may be described mathematically by delta functions at $\rho = a$ and $z = h$, as depicted in Fig. 6.10, $J_{s\phi} = \mathcal{I}\delta(\rho - a)\delta(z - h)$ and

$$\left(\frac{\partial^2}{\partial \rho^2} + \frac{1}{\rho}\frac{\partial}{\partial \rho} - \frac{1}{\rho^2} + \frac{\partial^2}{\partial z^2} - k^2\right) E_\phi = j\omega\mu\mathcal{I}\delta(\rho - a)\delta(z - h). \tag{6.49}$$

This is the equation governing the electric field due to a circular current loop with axis perpendicular to a half-space conductor, in the quasi-static regime.

Solution for E

The solution of (6.49) will be found by the method of separation of variables. Everywhere *off* the current loop, (6.49) may be written as

$$\left(\frac{\partial^2}{\partial\rho^2}+\frac{1}{\rho}\frac{\partial}{\partial\rho}-\frac{1}{\rho^2}+\frac{\partial^2}{\partial z^2}-k_i^2\right)E_\phi^i=0, \tag{6.50}$$

where $k_i^2=j\omega\mu_i\sigma_i$. The sub- or superscript i may take values 1, 2, and 3, and refers to regions above the loop ($z>h$), below the loop but above the conductor ($0<z<h$), and inside the conductor ($z\le 0$), respectively, as labeled in Fig. 6.10.

Suppose the solution is variable-separable, of the form $E_\phi^i(\rho,z)=R(\rho)Z_i(z)$. The form of (6.50) indicates that the radial part of the solution does not change from one region to another, so $R(\rho)$ needs no subscript. Substitute this form into (6.50) and divide by $R(\rho)Z_i(z)$ to obtain

$$\frac{1}{R(\rho)}\frac{\partial^2R(\rho)}{\partial\rho^2}+\frac{1}{\rho R(\rho)}\frac{\partial R(\rho)}{\partial\rho}-\frac{1}{\rho^2}+\frac{1}{Z_i(z)}\frac{\partial^2Z_i(z)}{\partial z^2}-k_i^2=0. \tag{6.51}$$

Variables have now been separated; terms in (6.51) depend either on ρ or on z. This means that (6.51) can be separated into two equations by introducing a variable of separation, κ, in the following way:

$$\frac{1}{R(\rho)}\frac{\partial^2R(\rho)}{\partial\rho^2}+\frac{1}{\rho R(\rho)}\frac{\partial R(\rho)}{\partial\rho}-\frac{1}{\rho^2}=-\kappa^2 \tag{6.52}$$

$$\frac{1}{Z_i(z)}\frac{\partial^2Z_i(z)}{\partial z^2}-k_i^2=\kappa^2. \tag{6.53}$$

Equation (6.52) is a first-order Bessel equation with general solution

$$R(\rho)=\int_0^\infty\alpha(\kappa)J_1(\kappa\rho)d\kappa, \tag{6.54}$$

where $J_1(u)$ is the Bessel function of the first kind, of order 1, and $\alpha(\kappa)$ is a function of the continuous variable κ whose form is determined according to the boundary conditions of the system. A term containing $Y_1(u)$, the Bessel function of the second kind, of order 1, is not needed because there is no source at $\rho=0$. A discussion of the properties of Bessel functions is given in the Appendix, Sect. 10.4. Since κ is a continuous variable, the electric field is obtained by integrating over the range of κ. Write (6.53) as

$$\frac{\partial^2Z_i(z)}{\partial z^2}-\gamma_i^2Z(z)=0 \tag{6.55}$$

where $\gamma_i = \sqrt{\kappa^2 + k_i^2}$ and the root with positive real part is taken. The general solution of (6.55) contains terms of the form $e^{\gamma_i z}$ and $e^{-\gamma_i z}$. Hence, combining with (6.54), the general solution of (6.51) may be written as

$$E_\phi^i(\rho, z) = R(\rho)Z_i(z) = \int_0^\infty \left[A_i(\kappa)e^{\gamma_i z} + B_i(\kappa)e^{-\gamma_i z}\right] J_1(\kappa\rho)d\kappa \tag{6.56}$$

where $\alpha(\kappa)$ has been incorporated into $A_i(\kappa)$ and $B_i(\kappa)$. Consider in turn each of the three regions labeled in Fig. 6.10. In region 1, above the current loop,

$$E_\phi^1(\rho, z) = \int_0^\infty B_1(\kappa)e^{-\kappa z} J_1(\kappa\rho)d\kappa. \tag{6.57}$$

In region 2, below the current loop but above the half-space,

$$E_\phi^2(\rho, z) = \int_0^\infty \left[A_2(\kappa)e^{\kappa z} + B_2(\kappa)e^{-\kappa z}\right] J_1(\kappa\rho)d\kappa, \tag{6.58}$$

and in region 3, the conductor,

$$E_\phi^3(\rho, z) = \int_0^\infty A_3(\kappa)e^{\gamma_3 z} J_1(\kappa\rho)d\kappa. \tag{6.59}$$

The coefficients are now determined by applying interface conditions (5.19) and (5.21) between regions 1, 2, and 3 (see Exercise 5 at the end of this chapter). Note that imposing continuity of the tangential component of the electric field (E_ϕ) is straightforward at both interfaces, whereas the presence of the coil filament comes into play in application of the condition on the tangential component of the magnetic field (H_ϕ). In fact, the resulting interface conditions on E_ϕ are

$$E_\phi^1(\rho, h) = E_\phi^2(\rho, h), \tag{6.60}$$

$$\frac{\partial}{\partial z}E_\phi^1(\rho, z)\bigg|_{z=h} = \frac{\partial}{\partial z}E_\phi^2(\rho, z)\bigg|_{z=h} + j\omega\mu\mathcal{I}\delta(\rho - a), \tag{6.61}$$

$$E_\phi^2(\rho, 0) = E_\phi^3(\rho, 0), \tag{6.62}$$

$$\frac{\partial}{\partial z}E_\phi^2(\rho, z)\bigg|_{z=0} = \frac{\partial}{\partial z}E_\phi^3(\rho, z)\bigg|_{z=0}. \tag{6.63}$$

Finally, the following expressions for E_ϕ^i are obtained:

$$E_\phi^1(\rho, z) = -\frac{1}{2}j\omega\mu_0\mathcal{I}a\int_0^\infty J_1(\kappa a)J_1(\kappa\rho)e^{-\kappa(h+z)}\left[e^{2\kappa h} + \frac{(\kappa - \gamma)}{(\kappa + \gamma)}\right]d\kappa, \tag{6.64}$$

$$E_\phi^2(\rho, z) = -\frac{1}{2} j\omega\mu_0 \mathcal{I} a \int_0^\infty J_1(\kappa a) J_1(\kappa\rho) e^{-\kappa h} \left[e^{\kappa z} + \frac{(\kappa - \gamma)}{(\kappa + \gamma)} e^{-\kappa z} \right] d\kappa, \tag{6.65}$$

$$E_\phi^3(\rho, z) = -j\omega\mu_0 \mathcal{I} a \int_0^\infty J_1(\kappa a) J_1(\kappa\rho) e^{-\kappa h + \gamma z} \frac{\kappa}{(\kappa + \gamma)} d\kappa. \tag{6.66}$$

In these equations, $\gamma_3 = \sqrt{\kappa^2 + j\omega\mu_3\sigma_3}$ is replaced by $\gamma = \sqrt{\kappa^2 + j\omega\mu_0\sigma}$ for simplicity, where the root with positive real part is taken and, as before, ω is angular frequency, $\mu_0 = 4\pi \times 10^{-7}$ H/m is the permeability of free space and σ is the conductivity of the test-piece.

An efficient way of evaluating the integrals in the above equations for E_ϕ is to truncate the domain of the electric field at a particular value of r, far from the loop, where it has decayed to approximately zero. Truncating at approximately ten times the coil radius usually gives sufficient accuracy. Then, the integral can be written in terms of a summation based on the set of zeros of the function $J_1(u)$. This technique is used extensively in [10] and references therein.

Calculation of Z

Now that the solution for $\mathbf{E}$ has been obtained, (6.64)–(6.66), the self-induced voltage in the current filament can be obtained by integrating $\mathbf{E}$ around the filament. The impedance can then be obtained by means of relation (4.25); $Z = \mathcal{V}/\mathcal{I}$. In general, the voltage induced by field $\mathbf{E}$ in a current filament is, in phasor form,

$$\mathcal{V} = -\int \mathbf{E} \cdot d\mathbf{l}, \tag{6.67}$$

where the path of the integral follows the current loop. In the case of the axially symmetric single loop shown in Fig. 6.10,

$$\mathcal{V} = -a \int_0^{2\pi} E_\phi(a, h) d\phi = -2\pi a E_\phi(a, h) \tag{6.68}$$

and $\mathcal{V}$ can be obtained immediately by inserting $E_\phi(a, h)$ from either (6.64) or (6.65) into (6.68). Dividing by $\mathcal{I}$ then gives the self-induced impedance of the current filament, Z^δ,

$$Z^\delta = j\omega\mu_0\pi a^2 \int_0^\infty [J_1(\kappa a)]^2 \left[1 + \frac{(\kappa - \gamma)}{(\kappa + \gamma)} e^{-2\kappa h} \right] d\kappa. \tag{6.69}$$

Examining (6.69) it is seen that Z^δ depends on the frequency of operation ω, the coil cross-sectional area πa^2, its position with reference to the sample, h, and the sample conductivity σ. The above relation has been derived on the assumption of a non-ferromagnetic test-piece, but if the conductor is ferromagnetic then

$$Z^{\delta} = j\omega\mu_0\pi a^2 \int_0^{\infty} [J_1(\kappa a)]^2 \left[1 + \frac{(\mu_r\kappa - \gamma)}{(\mu_r\kappa + \gamma)} e^{-2\kappa h}\right] d\kappa, \tag{6.70}$$

with $\gamma = \sqrt{\kappa^2 + j\omega\mu_0\mu_r\sigma}$, and Z^{δ} depends also on the relative permeability μ_r of the test-piece. By letting $h \to \infty$ the impedance of an isolated current filament, Z_0^{δ}, can be obtained readily:

$$Z_0^{\delta} = j\omega\mu_0\pi a^2 \int_0^{\infty} [J_1(\kappa a)]^2 d\kappa. \tag{6.71}$$

From (6.70), the self-inductance L of the coil can be obtained via (6.1). Similarly, the inductance L_0 of the isolated coil can be obtained from (6.71).

Comparing (6.71) with (6.70) allows the contribution to Z^{δ} from the test-piece to be identified, as follows:

$$Z^{\delta} = Z_0^{\delta} + j\omega\mu_0\pi a^2 \int_0^{\infty} [J_1(\kappa a)]^2 \frac{(\mu_r\kappa - \gamma)}{(\mu_r\kappa + \gamma)} e^{-2\kappa h} d\kappa. \tag{6.72}$$

6.3.4 Coil above a Half-Space Conductor

The impedance of a coil with finite cross section, shown in Fig. 6.11, is of more practical importance than that for the current loop obtained in the previous section, but can be obtained from it by the following process of superposition.

Electric Field

By the process of linear superposition, the fields due to n filamentary loops may be summed to obtain the total field due to a coil with n turns, $\mathbf{E}^T$, assuming that the current in each loop has the same phase and amplitude;

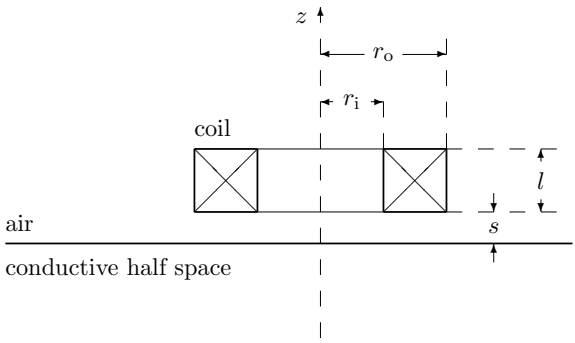

Fig. 6.11 Cross section through the axis of a circular, air-cored, eddy-current coil, positioned horizontally above a conductive half-space

$$\mathbf{E}^T(\rho, z) = \sum_{i=1}^{n} E(\rho, z|a_i, h_i) \tag{6.73}$$

where $E(\rho, z|a_i, h_i)$ is the electric field produced by the ith filamentary loop at $(a_\mathrm{s}, h_\mathrm{s})$. It is convenient to write this summation as an integral over the cross section of the coil. To do this, the superposition of the n δ-function coils must be approximated by a continuous current density $\mathbf{J}_\mathrm{s}(a_\mathrm{s}, h_\mathrm{s})$ over the coil cross section and

$$\mathbf{E}^T(\rho, z) = \int_{\text{coil cross section}} \mathbf{E}(\rho, z|a_\mathrm{s}, h_\mathrm{s}) dS, \tag{6.74}$$

where $\mathbf{E}(\rho, z|a_\mathrm{s}, h_\mathrm{s})$ is the electric field produced by the equivalent current density $\mathbf{J}_s$ in the coil and the subscript s indicates that this is the *source* current density. The variables a_s and h_s are, then, continuous variables in the radial and vertical directions, respectively. For a coil with rectangular cross section and parameters as shown in Fig. 6.11,

$$\mathbf{E}^T(\rho, z) = \int_{s}^{s+l} \int_{r_\mathrm{i}}^{r_\mathrm{o}} \mathbf{E}(\rho, z|a_\mathrm{s}, h_\mathrm{s}) da_\mathrm{s} dh_\mathrm{s}. \tag{6.75}$$

As an example of applying the process of linear superposition consider the electric field in the region above the coil. This corresponds to region 1 in the case of the circular current loop treated in Sect. 6.3.3 and shown in Fig. 6.10. Taking the result for $E_\phi^1(\rho, z)$ in the case of the δ-function coil, (6.64), and inserting that into integral (6.75) gives

$$E_\phi^{T,1}(\rho, z) = -\frac{1}{2} j\omega\mu_0 \mathcal{I} \int_0^\infty J_1(\kappa\rho) \left\{ \int_{r_\mathrm{i}}^{r_\mathrm{o}} a_\mathrm{s} J_1(\kappa a_\mathrm{s}) da_\mathrm{s} \times \right.$$
$$\left. \int_{s}^{s+l} e^{-\kappa(h_\mathrm{s}+z)} \left[e^{2\kappa h_\mathrm{s}} + \frac{(\kappa - \gamma)}{(\kappa + \gamma)} \right] dh_\mathrm{s} \right\} d\kappa, \tag{6.76}$$

where the order of integration has been reversed. Consider first the integral over a_s.

$$\int_{r_\mathrm{i}}^{r_\mathrm{o}} a_\mathrm{s} J_1(\kappa a_\mathrm{s}) da_\mathrm{s} = \frac{1}{\kappa^2} J(\kappa r_\mathrm{i}, \kappa r_\mathrm{o}) \tag{6.77}$$

where

$$J(x_1, x_2) = \int_{x_1}^{x_2} x J_1(x) dx = \frac{\pi}{2} x \left[J_0(x)\mathbf{H}_1(x) - J_1(x)\mathbf{H}_0(x) \right]_{x_1}^{x_2} \tag{6.78}$$

and $\mathbf{H}_n$ denotes the Struve function of order n. Guidance on computing $J(x_1, x_2)$ efficiently has been provided in [10]. Now consider terms in (6.76) that depend on h_s:

$$\int_s^{s+l} e^{-\kappa(h_s+z)} \left[e^{2\kappa h_s} + \frac{(\kappa-\gamma)}{(\kappa+\gamma)} \right] dh_s. \tag{6.79}$$

Integrating over this variable is easily accomplished analytically such that, finally,

$$E_\phi^{T,1}(\rho, z) = -\frac{1}{2} j\omega\mu_0 \mathcal{I} \int_0^\infty \frac{1}{\kappa^3} J(\kappa r_\mathrm{i}, \kappa r_\mathrm{o}) J_1(\kappa\rho) e^{-\kappa z} \left[e^{\kappa s}(e^{\kappa l} - 1) - e^{-\kappa s} \frac{(\kappa-\gamma)}{(\kappa+\gamma)} (e^{-\kappa l} - 1) \right] d\kappa. \tag{6.80}$$

Expressions for $E_\phi^{T,i}$, in other regions, may be obtained in a similar manner.

Voltage in a Surface Coil near a Half-Space Conductor

The total voltage induced in a coil of n turns is

$$\mathcal{V} = -2\pi \sum_{i=1}^{n} a_i E_\phi(a_i, h_i), \tag{6.81}$$

in which $2\pi a_i$ is the circumferential length and h_i is the height above the half-space of the ith current loop, and $E_\phi(a_i, h_i)$ is the electric field of that loop. It is convenient to approximate this summation by an integral over a turn density of N turns per unit cross-sectional area of the coil. To do this it will be assumed that there is a constant number of turns per unit cross-sectional area of the coil, such that

$$N = \frac{n}{l(r_\mathrm{o} - r_\mathrm{i})} \tag{6.82}$$

where the notation of Fig. 6.11 is employed. Then,

$$\mathcal{V} = -\frac{2\pi n}{l(r_\mathrm{o} - r_\mathrm{i})} \int_s^{s+l} \int_{r_\mathrm{i}}^{r_\mathrm{o}} a_\mathrm{s} E_\phi(a_\mathrm{s}, h_\mathrm{s}) da_\mathrm{s} dh_\mathrm{s}. \tag{6.83}$$

Z for Surface Coil near a Half-Space Conductor

An expression for the impedance of the surface coil near a half-space conductor is now calculated using relation (4.25); $Z = \mathcal{V}/\mathcal{I}$, with $\mathcal{V}$ given by (6.83). Note, the current density of the source in the case of the finite coil is $J_\mathrm{s} = n\mathcal{I}/[l(r_\mathrm{o} - r_\mathrm{i})]$, not to be confused with $J_\mathrm{s} = \mathcal{I}\delta(\rho - a)\delta(z - h)$ as for the infinitesimal current loop. This must be reflected in the expression for E_ϕ since $\mathbf{E}$ and $\mathbf{J}$ are related according to the point form of Ohm's Law, relation (2.15). Effectively, $\mathcal{I}$ in E_ϕ as expressed in (6.64) or (6.65) should be replaced by $n\mathcal{I}/[l(r_\mathrm{o} - r_\mathrm{i})]$ in the case of the finite coil so that

$$Z = -\frac{2\pi n^2}{l^2(r_\mathrm{o} - r_\mathrm{i})^2} \int_s^{s+l} \int_{r_\mathrm{i}}^{r_\mathrm{o}} a_\mathrm{s} E_\phi(a_\mathrm{s}, h_\mathrm{s}) da_\mathrm{s} dh_\mathrm{s}. \tag{6.84}$$

Now the integrals with respect to a_s and h_s may be evaluated by inserting $E_\phi(a_\mathrm{s}, h_\mathrm{s})$ into (6.84). To do this, the integral over h_s is split into regions within the coil below and above h_s. In the region above h_s the expression for $E^1_\phi(\rho, z)$ is inserted whereas in the region below h_s the expression for $E^2_\phi(\rho, z)$ is used. Explicitly,

$$Z = -\frac{2\pi n^2}{l^2(r_\mathrm{o} - r_\mathrm{i})^2} \int_{r_\mathrm{i}}^{r_\mathrm{o}} a_\mathrm{s} \left[\int_s^{h_\mathrm{s}} E^2_\phi(a_\mathrm{s}, h_\mathrm{s}) dh_\mathrm{s} + \int_{h_\mathrm{s}}^{s+l} E^1_\phi(a_\mathrm{s}, h_\mathrm{s}) dh_\mathrm{s} \right] da_\mathrm{s}. \tag{6.85}$$

Inserting expressions for $E^1_\phi(\rho, z)$ and $E^2_\phi(\rho, z)$, the following integrals with respect to a_s and h_s emerge:

$$Z = \frac{j\omega\mu_0\pi n^2}{l^2(r_\mathrm{o} - r_\mathrm{i})^2} \int_0^\infty \int_{r_\mathrm{i}}^{r_\mathrm{o}} [a_\mathrm{s} J_1(\kappa a_\mathrm{s})]^2 \, da_\mathrm{s} \int_s^{s+l} \left[1 + \frac{(\kappa - \gamma)}{(\kappa + \gamma)} e^{-2\kappa h_\mathrm{s}} \right] dh_\mathrm{s} d\kappa, \tag{6.86}$$

assuming that the current in each loop has the same phase and amplitude.

Treating the integrals in (6.86) as outlined in (6.77)–(6.79) gives the following expression for the impedance of an air-cored surface coil of finite cross section near a conductive half-space:

$$Z = \frac{j\omega\mu_0\pi n^2}{l^2(r_\mathrm{o} - r_\mathrm{i})^2} \int_0^\infty \frac{J^2(\kappa r_\mathrm{i}, \kappa r_\mathrm{o})}{\kappa^5} \left(2l + \frac{1}{\kappa} \left\{ 2e^{-\kappa l} - 2 + [e^{-2\kappa(l+s)} + e^{-2\kappa s} - 2e^{-\kappa(l+2s)}] \left(\frac{\gamma - \kappa}{\gamma + \kappa} \right) \right\} \right) d\kappa. \tag{6.87}$$

Note, Z depends on the frequency of operation of the probe, ω, the coil dimensions, r_i, r_o and l, the *square* of the number of turns, n^2 (as in the case of the long solenoid, Exercise 3 at the end of this chapter), the coil position with reference to the sample, s, and the sample conductivity, σ. If the conductive half-space is also ferromagnetic, with relative permeability μ_r, then $\gamma = \sqrt{\kappa^2 + j\omega\mu_0\mu_\mathrm{r}\sigma}$ and the last term in (6.87) is $(\gamma - \mu_\mathrm{r}\kappa)/(\gamma + \mu_\mathrm{r}\kappa)$.

By letting $s \to \infty$ in (6.87), the following expression for the impedance of an isolated coil is obtained,

$$Z_0 = \frac{2j\omega\mu_0\pi n^2}{l^2(r_\mathrm{o} - r_\mathrm{i})^2} \int_0^\infty \frac{J^2(\kappa r_\mathrm{i}, \kappa r_\mathrm{o})}{\kappa^5} \left(l + \frac{e^{-\kappa l} - 1}{\kappa} \right) d\kappa. \tag{6.88}$$

From relation (6.87), the self-inductance of the loop L can be deduced via relation (6.1). Similarly, from (6.88) the inductance of the isolated loop L_0 can be obtained. Taking (6.87) and (6.88) together, the contribution to the coil impedance of the test-piece can be isolated.

$$Z = Z_0 + \frac{j\omega\mu_0\pi n^2}{l^2(r_\mathrm{o} - r_\mathrm{i})^2} \int_0^\infty \frac{J^2(\kappa r_\mathrm{i}, \kappa r_\mathrm{o})}{\kappa^6} [e^{-2\kappa(l+s)} + e^{-2\kappa s} - 2e^{-\kappa(l+2s)}] \left(\frac{\gamma - \kappa}{\gamma + \kappa} \right) d\kappa. \tag{6.89}$$

Evaluation of (6.87), or of (6.89) with (6.88), for particular coil parameters r_i, r_o, l and n^2 allows calculation of impedance values such as those plotted as an impedance-plane plot in Fig. 6.2, in which the effect of different material conductivities, and of coil frequency, are illustrated. The impedance-plane plot of Fig. 6.3 illustrates the effect of varying frequency, lift-off and permeability although for this figure the impedance is plotted in normalized form, as Z/X_0.

6.3.5 Ferrite Core

The strength of coupling between an eddy-current surface probe and the test-piece can be increased by winding the coil around a ferrite core, rather than a purely dielectric material such as machinable plastic. Ferrite cores are commonly used for increasing the signal-to-noise ratio of a particular coil configuration. A schematic diagram of a coil wound around a ferrite core is shown in Fig. 6.12. The ferrite strengthens the magnetic flux density within the coil in proportion to the permeability of the ferrite, (2.25) and (4.16), and consequently strengthens the electromagnetic coupling between the probe coil and the test-piece. Ferrites are low conductivity but high-permeability ferromagnetic materials. It is important that the core material has low conductivity because, if it were conductive, eddy currents would be induced by the coil in the core, as well as in the test-piece. The eddy currents induced in a conductive core would have the counterproductive effect of *reducing* the eddy-current density in the test-piece, which must be avoided.

Manganese zinc (MnZn) ferrite is commonly used in eddy-current probe cores and in transformer cores, where it is also desirable to minimize energy losses that would reduce the efficiency of the transformer. The initial relative permeability of MnZn ferrite is on the order of 1,000. The resistivity of MnZn ferrite is a function of temperature and frequency. Resistivity is reduced as temperature increases, and as frequency increases. Example values of the resistivity of MnZn ferrite are given in Table 6.2.

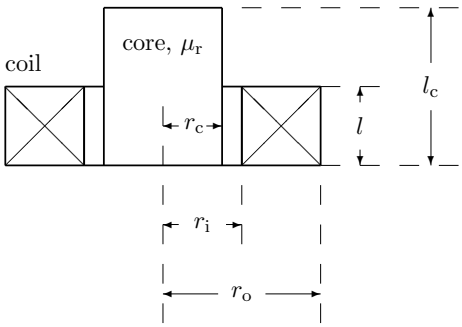

Fig. 6.12 Cross section through the axis of a circular, ferrite-cored, eddy-current coil

Table 6.2 Resistivity as a function of frequency for MnZn ferrites [11]

Frequency (MHz)	Resistivity (Ωm)
0.1	≈2
1	≈0.5
10	≈0.1
100	≈0.01

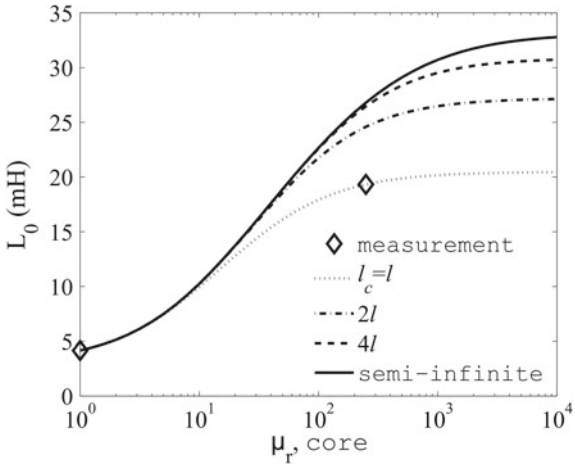

Fig. 6.13 Self-inductance of an isolated ferrite-cored coil as a function of μ_r of the core, for core lengths $l_c = l, 2l, 4l$ and for a semi-infinite core

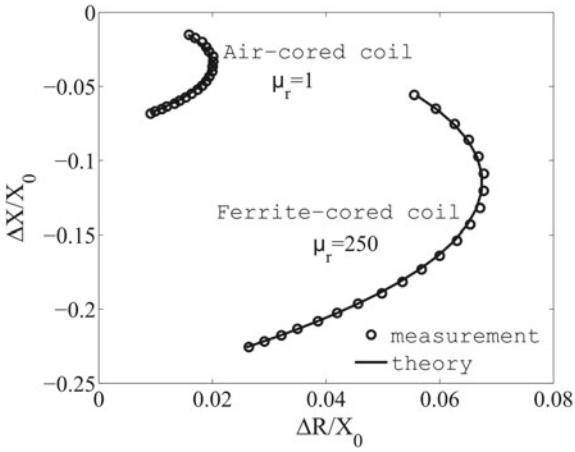

Fig. 6.14 Normalized impedance-plane diagram comparing Z for an air-cored and a ferrite-cored coil above a conductive half-space, where $\Delta X = X - X_0$ and $\Delta R = R - R_0$

Theodoulidis [12] and Lu et al. [13] have analyzed the impedance of a ferrite-cored coil utilizing the truncated region eigenfuction expansion (TREE) method, Sect. 7.3.1. Using this approach, the curves presented in Figs. 6.13 and 6.14 have been calculated. Parameters of the coil, core and conductive half-space used to obtain the calculated data plotted in Figs. 6.13 and 6.14 are given in Table 6.3. In Fig. 6.13 the self-inductance of an isolated ferrite-cored coil is plotted as a function of the relative permeability of the ferrite, and for various core lengths. It can be seen that

Table 6.3 Parameters for the numerical calculations whose data are presented in Fig. 6.13 and Fig. 6.14. Note that the core length and test-piece parameters are relevant only to Fig. 6.14

Coil parameters		Value	Ferrite core parameters		Value
r_o	Outer radius (mm)	10.275	r_c	Core radius (mm)	3.880
r_i	Inner radius (mm)	5.025	l_c	Core length (mm)	29.95
l	Length (mm)	18.180			
s	Coil stand-off (mm)	2.650	Test-piece parameters		
h	Probe lift-off (mm)	0.590	σ	Conductivity (MSm^{-1})	20.40
n	Number of turns	776	μ_r	Relative permeability	1

L_0 increases rapidly at first, as $\mu_{r,core}$ increases, but the improvement is only slight as $\mu_{r,core}$ increases above about 100. Similarly, there is a rapid increase in L_0 as the core length is doubled with respect to the coil length, but lesser improvement is obtained as the core length is doubled again and then made semi-infinite.

Figure 6.14 reveals the enhancement in Z and coupling parameter c, (6.3), when a ferrite core with $\mu_r = 250$ is inserted into the coil. One way of thinking about the effect of the ferrite core on the coupling between the coil and the test-piece is that the introduction of a ferrite core into a surface coil has an effect similar to that of moving the coil windings closer to the test-piece.

6.3.6 Sources of Uncertainty

Nonideal Coil Behavior

It has been discussed in previous sections that an ideal eddy-current coil would be a pure inductor. The inductance of the coil is the important circuit property as far as inducing current in a test-piece is concerned, and in detecting perturbations in the magnetic field associated with the induced eddy currents, due to the presence of defects. The behavior of a real coil is not that of a pure inductor, due in part to the fact that the current flowing in an eddy-current coil is not uniformly distributed over the cross section of the coil. The current is restricted to flow within the coil windings and, in fact, near the surface of the windings for higher frequency excitations (a consequence of the skin effect). These geometrical restrictions on the current density causes the coil to exhibit inter-winding capacitance. In addition, a real eddy-current coil exhibits finite DC resistance due to the resistivity of the metal constituting the coil windings, usually copper. Additional perturbations to the current density in the coil arise from irregularity in the windings. Capacitance in the leads connecting the probe to the power source also makes a significant contribution to the probe impedance at higher frequencies.

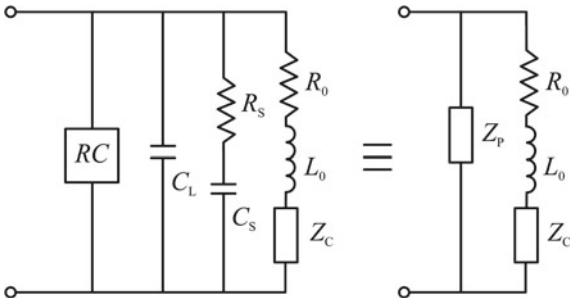

Fig. 6.15 Equivalent electrical circuit for an eddy current probe coil. R_0 and L_0 represent the DC resistance and inductance of the probe coil, respectively. Z_C is the impedance due to coupling with an external conductor (the test-piece). R_S and C_S represent stray resistance and capacitance, respectively, in the coil windings. C_L accounts for capacitance in the leads connecting the probe with the power source. Any other unspecified contributions to the impedance of the electrical circuit are represented by RC. In the right-hand figure, all parallel circuit components are lumped together in one parallel impedance, Z_P [14]

An equivalent circuit that takes into account these various contributions to the impedance of a real eddy current probe is shown schematically in Fig. 6.15 [14]. This circuit is more complicated than those considered in Chap. 4 but one familiar feature is that due to the presence of capacitive elements in parallel with series inductance and resistance, the probe resonates at a certain frequency f_0. Resonance manifesting in measured R and L is shown in Fig. 6.16 for one particular coil [14]. The value of f_0 depends on the values of the different circuit components in each individual coil, but f_0 on the order of hundreds of kHz is typical for an eddy-current coil. In order to avoid large uncertainties in precision eddy current measurements, a rule of thumb is that the operating frequency of a probe should be less than one-third of the resonance frequency.

In a routine EC inspection, the nonideal behavior of an EC coil is assumed to be negligible provided that it is operated at a frequency sufficiently far below f_0. For benchmark experiments in EC research, however, whose purpose is to provide data that validates a new theoretical treatment of a particular EC inspection, agreement between theory and experiment is sought to within a few percent. Under these circumstances it is essential to correct for the nonideal behavior of the coil. A procedure by which corrections for the nonideal coil behavior can be made was published by Harrison, Jones, and Burke in 1996 [14]. To follow this procedure for an eddy-current coil is in fact to *characterize* that coil since, during the correction procedure, *effective* values for the coil's outer radius and stand-off are determined. Essential steps in the correction procedure are explained in the following two paragraphs for an air-cored surface coil above a metal plate. The procedure is not restricted to this probe and test-piece configuration, however, but may be adapted to work for other canonical configurations for which impedance formulas are available [10].

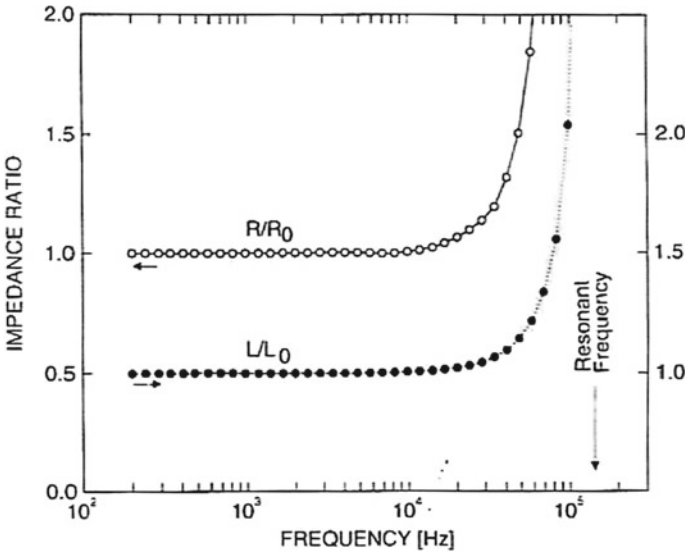

Fig. 6.16 Resistance and inductance of a coil, normalized with respect to the DC values, are shown as a function of operating frequency. Resonance is observed at 142 kHz for this particular coil [14]. With kind permission from Springer Science and Business Media: *J. Nondestr. Eval.*, vol. 15, 1996, p. 26, Benchmark problems for defect size and shape determination in eddy-current nondestructive evaluation, D. J. Harrison, L. D. Jones, and S. K. Burke, Fig. 4. Original caption: Isolated coil inductance and resistance as a function of frequency. Deviations from the DC values are due to nonideal coil behavior. The isolated coil resonant frequency is indicated by an arrow

Correction for DC Coil Resistance and Stray Capacitance Following the method described in [14], the first step in making corrections for nonideal coil behavior is to adjust experimental impedance measurements to eliminate the effects of stray capacitance and DC resistance of the coil. The ideal admittance, obtained from the DC values of coil resistance and inductance, R_0 and L_0 respectively, is

$$Y_{\text{ideal}} = \frac{1}{Z_{\text{ideal}}} = \frac{1}{R_0 + j\omega L_0}. \tag{6.90}$$

Writing Y_0 as the experimentally measured admittance in air, where

$$Y_0^{\text{exp}} = \frac{1}{Z_0^{\text{exp}}}, \tag{6.91}$$

and subtracting Y_{ideal} gives the admittance of the equivalent parallel network, Y_{P}, where

$$Y_{\text{P}} = Y_0^{\text{exp}} - Y_{\text{ideal}}. \tag{6.92}$$

Denoting the uncorrected impedance of the coil, measured with the coil over the conductive plate, by $Z_{\mathrm{U}}^{\mathrm{exp}}$ (with associated admittance $Y_{\mathrm{U}}^{\mathrm{exp}}$), the corrected impedance $Z_{\mathrm{C}}^{\mathrm{exp}}$ is obtained by subtracting the effect of the parallel circuit,

$$Z_{\mathrm{C}}^{\mathrm{exp}} = \frac{1}{Y_{\mathrm{U}}^{\mathrm{exp}} - Y_{\mathrm{P}}}. \tag{6.93}$$

The corrected impedance change in the coil due to the plate, $\Delta Z_{\mathrm{C}}^{\mathrm{exp}}$, is therefore

$$\Delta Z_{\mathrm{C}}^{\mathrm{exp}} = Z_{\mathrm{C}}^{\mathrm{exp}} - Z_{\mathrm{ideal}}. \tag{6.94}$$

In the case that this correction procedure is not followed, the impedance change in the coil due to the plate is given by

$$\Delta Z_{\mathrm{U}}^{\mathrm{exp}} = Z_{\mathrm{U}}^{\mathrm{exp}} - Z_{\mathrm{ideal}}. \tag{6.95}$$

Effective Coil Parameters and Determination of Plate Conductivity Calculating the self-inductance of an isolated EC coil using (6.88) and (6.1), with macroscopically measured coil dimensions r_{i}, r_{o} and l as inputs, yields a value for L_0 that is typically a few percent higher than the value measured using an impedance analyzer or other instruments [15]. The discrepancy can be explained by arguing that the measured value of r_{o} overestimates the equivalent value for an ideal coil, since it represents the outermost extent of the windings of a nonuniform current distribution. An equivalent but uniform current distribution would occupy a smaller volume than the real, nonuniform current distribution in the coil. Perfect agreement between the calculated and measured values of L_0 can be obtained by introducing an effective value for the coil outer radius, $r_{\mathrm{o}}^{\mathrm{eff}} < r_{\mathrm{o}}$. In the correction procedure, the value of $r_{\mathrm{o}}^{\mathrm{eff}}$ is determined by varying its value in the calculation of L_0 until agreement with the measured value is achieved.

Again due to nonuniformity of the current density in the coil, it is anticipated that the measured stand-off of the coil will be smaller than that of an ideal coil for which other parameters are identical. The coil impedance Z depends strongly on s which means that this subtle effect is important if precise results are sought. An effective value of the coil stand-off may be determined by minimizing the root mean square (RMS) error between the experimentally measured impedance of the coil on a metal plate, and values calculated using (6.87). The RMS error, ε, is computed from the following relation, in which the superscript "exp" denotes experimentally measured values, and "thry" denotes theoretically calculated values. N is the number of frequency points.

$$\varepsilon^2 = \frac{1}{N}\sum_{j=1}^{N}\left\{\left[\frac{\Delta R_j^{\mathrm{exp}}(f_j) - \Delta R_j^{\mathrm{thry}}(f_j)}{\Delta R_j^{\mathrm{exp}}(f_j)}\right]^2 + \left[\frac{\Delta L_j^{\mathrm{exp}}(f_j) - \Delta L_j^{\mathrm{thry}}(f_j)}{\Delta L_j^{\mathrm{exp}}(f_j)}\right]^2\right\} \tag{6.96}$$

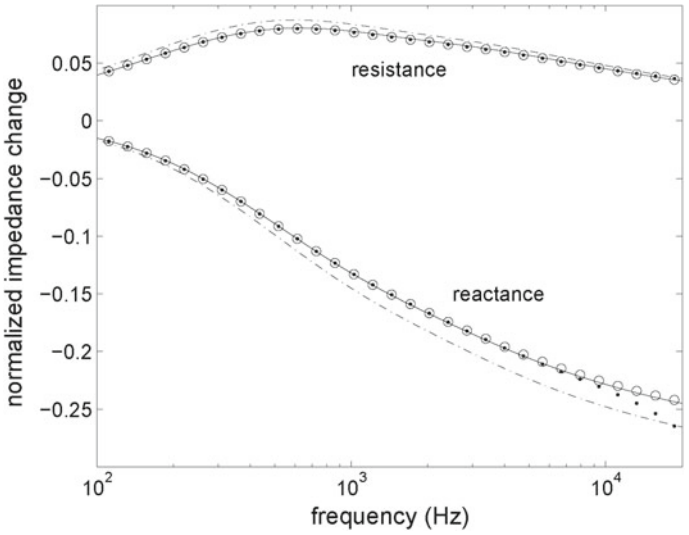

Fig. 6.17 Change in coil impedance due to a brass plate, normalized to the ideal isolated coil reactance $X_0 = \omega L_0$. Circles (o) represent experimental data corrected for nonideal coil behavior. Dots (·) represent uncorrected experimental data. Solid lines (—) represent theory with effective parameters. Broken lines (- - -) represent theory with measured parameters [15]. From: Bowler, N., Huang, Y.: Electrical conductivity measurement of metal plates using broadband eddy-current and four-point methods. Meas. Sci. Technol. **16**, 2193-2200 (2005), Fig. 2. ©IOP Publishing. Reproduced with permission. All rights reserved

At the same time, the conductivity of the plate is permitted to vary until ε is minimized. The probe stand-off and plate conductivity may be found simultaneously since ε shows well-defined minima with respect to variations in both of these parameters [14], especially at higher frequencies, Fig. 6.2.

In Fig. 6.17, the corrected experimental data, $\Delta Z_{\mathrm{C}}^{\mathrm{exp}}$ of (6.94), and uncorrected experimental data, $\Delta Z_{\mathrm{U}}^{\mathrm{exp}}$ of (6.95), are shown for normalized coil impedance change of a surface coil on a brass plate. For full details of this study see [15]. Also shown in Fig. 6.17 are curves calculated using (6.87) with measured and effective parameters. The improvement in agreement between theory and experiment after making corrections for DC coil resistance and stray capacitance, and refining coil parameters r_{o} and s, is dramatic. In Table 6.4, effective parameters obtained by this procedure for measurements on brass and stainless steel plates are compared with dimensions measured using digital calipers and conductivities measured using a Zetec MIZ-21A eddy-current instrument [15]. Notice that the effective outer radius is slightly smaller, and the effective stand-off is slightly greater, than values measured with calipers. This is in keeping with the initial hypothesis that an equivalent but uniform current distribution occupies a smaller volume than the real, nonuniform current distribution in the coil. The uncertainties in the effective value of s and in the fitted value of σ, quoted in Table 6.4, were assumed to be given by the RMS error ε, as defined in

Table 6.4 Measured and effective (or fitted) parameters. Lengths were measured using digital calipers at appropriate stages during fabrication of the coil. Conductivity σ was measured using a Zetec MIZ-21A eddy-current instrument

Parameter		Measured	Effective (geometric) and fitted (material)
r_o	Outer radius (mm)	11.84 ± 0.01	11.43 ± 0.06
s	Stand-off (mm)		
	Brass	1.00 ± 0.04	1.06 ± 0.03
	Stainless steel	1.00 ± 0.04	1.01 ± 0.02
σ	Conductivity (MSm^{-1})		
	Brass	16.2 ± 0.3	16.6 ± 0.4
	Stainless steel	0.7 ± 0.3	1.31 ± 0.02

(6.96), for each plate. Regarding the significant difference between the measured and fitted values of σ in stainless steel, given in Table 6.4, an independent measurement of conductivity by a four-point alternating current potential drop method on the same sample gave result $1.369 \pm 0.007\ \mathrm{MSm}^{-1}$ [15].

Geometrical Sources of Uncertainty

Probably the most significant source of uncertainty in impedance measurements made using an EC probe operating in absolute mode is the variation in distance between the probe coil and the test-piece that may occur as the probe scans the object surface. For a flat test-piece, this variation in probe and part separation may be described as a variation in the probe lift-off and is often termed *lift-off noise*. Such impedance changes are indicated in the impedance-plane plot of Fig. 6.3 which may be calculated using the theory of Dodd and Deeds [8], Sect. 6.3.4.

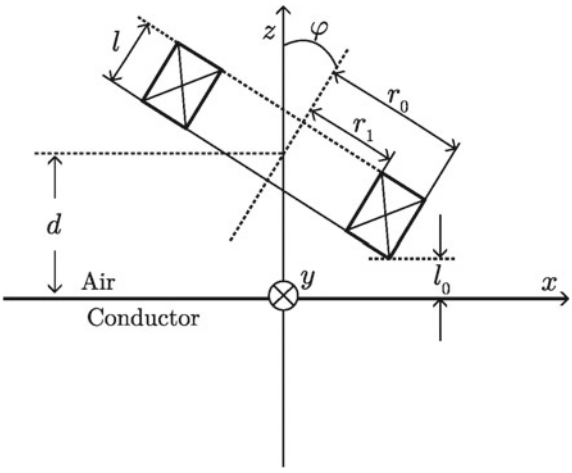

Fig. 6.18 Schematic diagram of surface EC coil whose axis is tilted at angle φ with respect to the direction normal to the test-piece surface

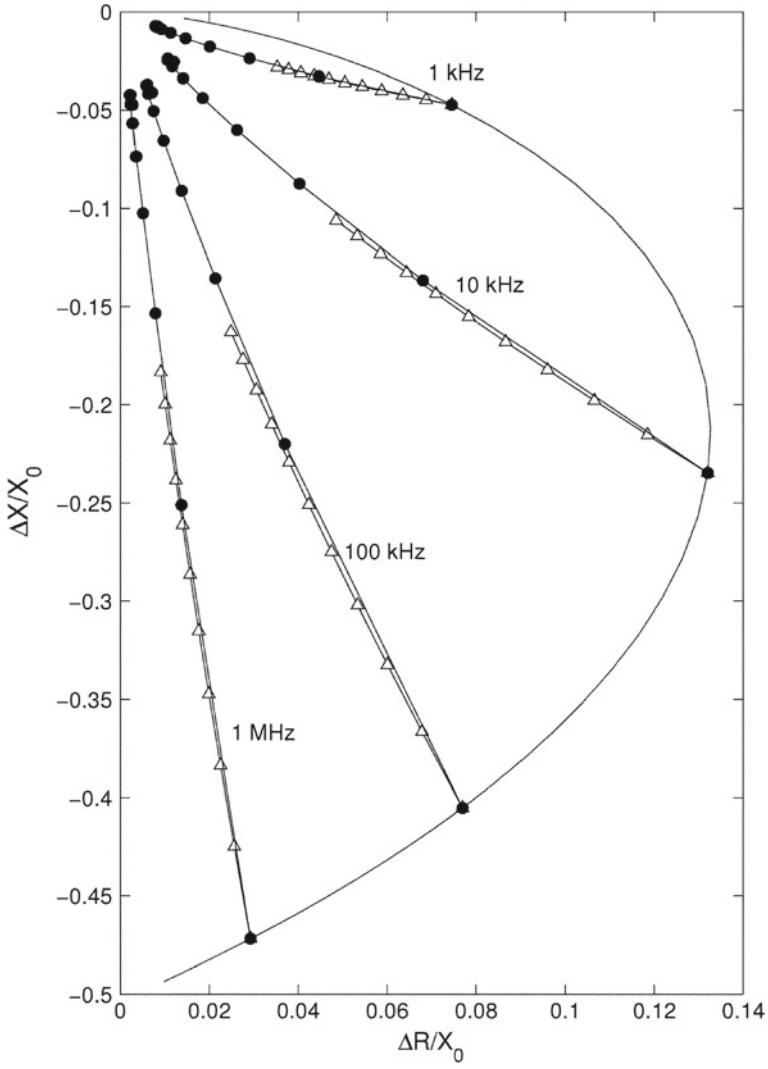

Fig. 6.19 Normalized impedance-plane plot as a function of coil tilt angle φ. Coil and test-piece parameters for the calculation are listed in Table 6.5. Note that in the axis labels ΔX here is equivalent to X and ΔR here is equivalent to $R - R_0$ as defined in (6.2). Reproduced with permission from IEEE: *IEEE Trans. Magn.*, vol. 41, 2005, p. 2453, Analytical model for tilted coils in eddy-current nondestructive inspection, T. Theodoulidis, Fig. 8. Original caption: Impedance change display showing tilt (•) and lift-off curves (△) in steps of 10° and 0.1 mm, respectively. The arc-shaped curve is produced by varying excitation frequency at zero lift-off and zero tilt angle

Table 6.5 Parameters for the numerical calculations whose data are presented in Figs. 6.19 and 6.20

Coil parameters		Value
r_o	Outer radius (mm)	4
r_i	Inner radius (mm)	2
l	Length (mm)	2
h	Lift-off (mm)	1
n	Number of turns	400
Test-piece parameters		
σ	Conductivity (MSm^{-1})	18.72
μ_r	Relative permeability	1

A similar source of noise in the signal of an absolute surface probe is *tilt* of the probe axis through an angle φ with respect to the direction normal to the surface of the test-piece, as shown schematically in Fig. 6.18. Tilt commonly occurs when a probe is scanned in contact with the test-piece because the friction between the probe and test-piece drags upon the probe base, causing the probe to tilt toward the direction of motion. In the context of Fig. 6.18 this would mean that the probe is being moved to the right. Theodoulidis analyzed the impedance of a tilted probe [16] and produced the impedance-plane plot shown in Fig. 6.19 for a coil and test-piece whose parameters are listed in Table 6.5. From the figure, it can be seen that the frequency response of Z at a particular angle of tilt gives rise to the same kind of curve that we are familiar with from the impedance-plane plot for the normal coil, Fig. 6.3. In Fig. 6.19, increasing the angle of tilt has a very similar effect on Z as increasing lift-off, which is also plotted.

In Fig. 6.20, eddy current amplitude and streamlines are plotted for a coil tilted at 0, 30, 60 and 90° with respect to the normal to the test-piece surface. It can be seen that the induced eddy currents become concentrated in the region directly below the coil edge for $\varphi = 90°$. This is the tangent coil configuration, which will be discussed further in Sect. 6.4.

Another source of uncertainty in impedance measurements is the presence of geometrical features in the test-piece, close to the inspection region. Examples of these are edges, joints, rivets, metal support structures and rapid changes in geometry such as corners. At worst, signals from these features completely mask the signal from the sought defect, rendering it undetectable. Often it is necessary to adjust the inspection frequency and choice of probe in order to minimize the signal from geometrical features that may mask the presence of defects. Coil impedance changes due to certain geometrical features are discussed in detail in Sect. 7.3.

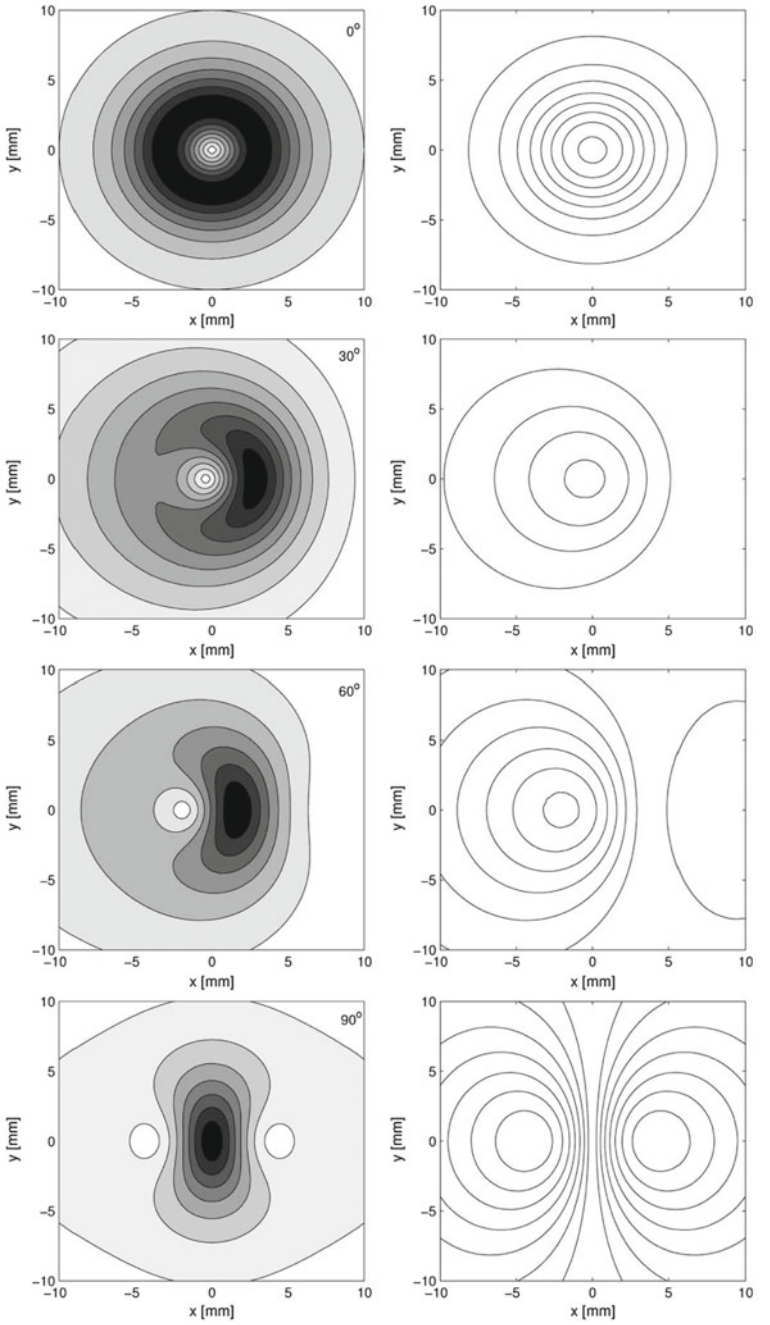
0°
30°
60°
90°
x [mm]
y [mm]
10
5
0
−5
−10

◀**Fig. 6.20** Eddy-current amplitude (left) and streamlines (right) by a coil tilted clockwise at 0 (top), 30, 60 and 90° (bottom) to the test-piece surface. Coil and test-piece parameters for the calculation are listed in Table 6.5. Reproduced with permission from IEEE: *IEEE Trans. Magn.*, vol. 41, 2005, p. 2451, Analytical model for tilted coils in eddy-current nondestructive inspection, T. Theodoulidis, Fig. 6. Original caption: Amplitude contours (left) and streamlines (right) of eddy currents induced on the surface of a conductive half-space by a cylindrical coil at various tilt angles. Coil rotation is clockwise

6.4 Tangent Coil

The tangent coil is oriented such that its axis lies parallel with the surface of the test-piece, as shown in Fig. 6.21. This is equivalent to tilting the axis of a surface coil through $\varphi = 90°$, Fig. 6.18. Referring to Fig. 6.20 it can be seen that the current density in the test-piece below a single tangent coil is concentrated below the coil windings, and is largely unidirectional in that region. Tangent coils are much less widely used than surface coils due to their significantly poorer coupling with the test-piece, but they find special application in plus-point probes, which combine two tangent coils. The plus-point probe is discussed in Sect. 8.5.

The solution by which the impedance of a tangent coil can be calculated is a limiting case of the solution for a tilted coil, which has been analyzed by Theodoulidis as mentioned in Sect. 6.3.6. Due to the lesser practical importance of the tangent coil configuration, when compared with the surface- and encircling-coil configurations, the full theoretical details of the impedance calculation for the tangent coil are not provided here. It can be observed from Fig. 6.19, however, that the calculated normalized impedance change is reduced by a factor of approximately 10 when a coil is tilted through 90° from the surface- to the tangent coil configuration. The interested reader is referred to [10] and [16] for further information.

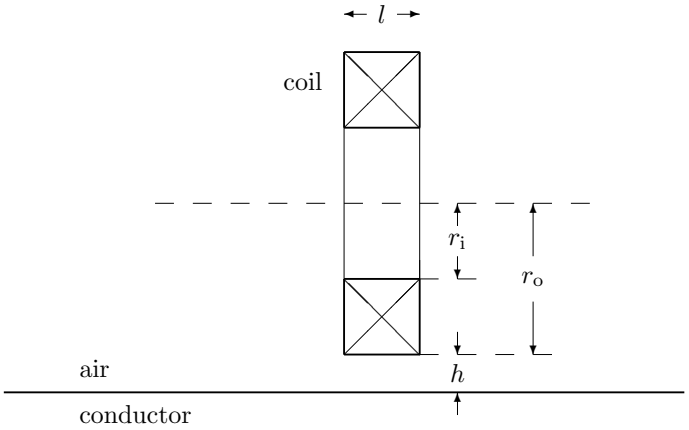

Fig. 6.21 Cross section through the axis of a circular, air-cored, eddy-current tangent coil, positioned above a conductive half-space

6.5 Encircling Coil

Encircling coils couple strongly with rod-like specimens, inducing eddy currents that flow in an azimuthal direction (circularly) around the rod. The probe is designed such that the test-piece may be passed through the middle of the coil, as shown in Fig. 6.22.

The cylindrical test-piece geometry was studied extensively by Friedrich Förster during the 1940s and beyond. Förster was a visionary who, during a study of ferromagnetic properties of metals in 1937, observed the influence of the earth's magnetic field on a test coil. This led Förster to develop highly sensitive measuring equipment for magnetic fields, the scientific basis for which was put into place in the 1950s and earned him the Victor de Forest Award in 1957. A summary of Förster's work relevant to the encircling coil is given in [17, Sect. 5: Analysis of encircling coil tests of wire, rods and bars].

In contrast with the surface coil and test-piece geometry, there is no lift-off associated with the encircling coil. Instead, the *fill factor*, η, indicates the fraction of the cross-sectional area of the coil that is occupied by the test object:

$$\eta = \left(\frac{\rho_1}{r_\mathrm{i}}\right)^2, \tag{6.97}$$

where ρ_1 is the radius of the cylindrical test-piece and r_i is the inner radius of the encircling coil. If the encircling coil is concentric with the test-piece, then the fill factor is an indicator of the strength of coupling between the coil and the test-piece. In Fig. 6.23, an example impedance-plane plot for a coil encircling a long, non-ferromagnetic, cylindrical rod is shown. Note that this impedance-plane diagram is

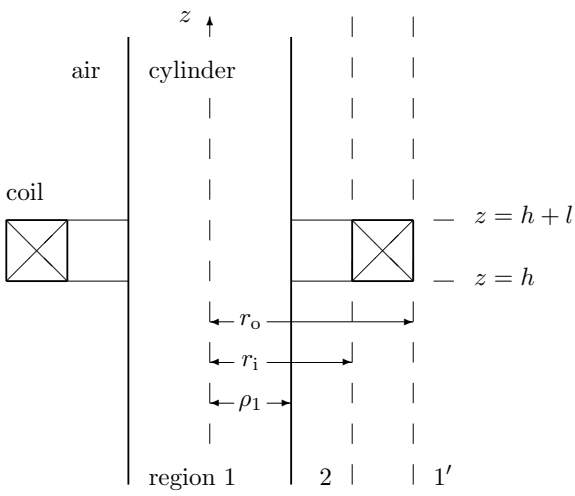

Fig. 6.22 Cross section through the axis of a circular coil with finite cross section, coaxial with a solid metal circular cylinder (test-piece)

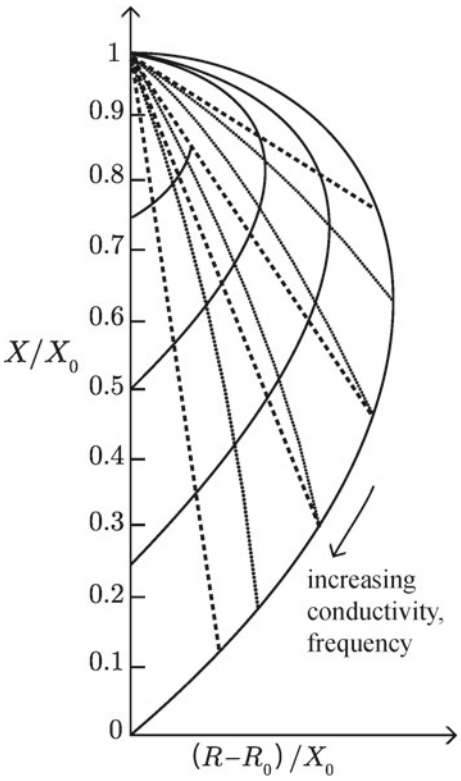

Fig. 6.23 Normalized impedance-plane plot for a coil with inner radius r_i encircling a cylindrical, non-ferromagnetic test-piece with radius ρ_1. Solid lines (——) represent the complex impedance of the probe as a function of rod conductivity, σ, or frequency, f. Broken lines (- - -) represent the effect of increasing the radius of the encircling coil r_i. Dotted lines (· · ·) indicate the effect of changing the sample radius ρ_1

presented in a form in which the data is normalized with respect to the reactance of the isolated coil, X_0. Comments made around (6.2) on the general shape of the normalized impedance-plane plot for a surface coil above a half-space conductor, Fig. 6.3, are applicable here. Figure 6.23 allows us to predict the way in which the coil impedance changes if either the sample diameter varies or a coil with different diameter is used. The outer curved solid line shows the locus of impedance values of a coil when it is tight to the test-piece (when the test-piece fills the coil and $\eta = 1$). The arrow indicates the way in which the impedance changes as either the test-piece conductivity or the frequency of the test are increased. From any fixed point on the outer solid curve, defined by particular values of frequency and conductivity, the dashed lines show how the impedance of the coil changes ($|Z|$ decreases) as the coil diameter increases, and the dotted lines show how $|Z|$ decreases as the diameter of the test-piece decreases.

In Fig. 6.24, an example impedance-plane plot for a coil encircling a long, ferromagnetic, cylindrical rod is shown. As for Fig. 6.23, this impedance-plane diagram is presented in a form in which the data is normalized with respect to the reactance of the isolated coil, X_0. Again, the arrow indicates the way in which the impedance changes as either the test-piece conductivity or the frequency of the test is increased.

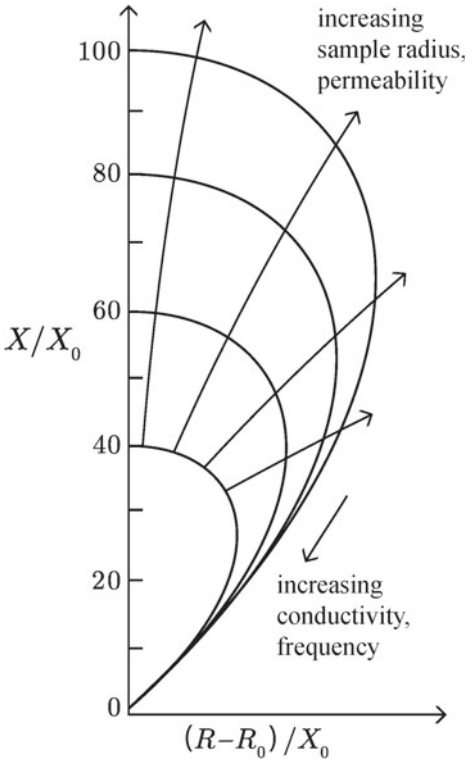

Fig. 6.24 Normalized impedance-plane plot for a coil with inner radius r_i encircling a cylindrical, ferromagnetic test-piece with radius ρ_1. Solid lines (——) represent the complex impedance of the probe as a function of rod conductivity, σ, or frequency of the test, f. Arrows (→) represent the effect of increasing the radius of the test-piece ρ_1, or the test-piece relative permeability [17]

A major difference between these curves and those for the case of non-ferromagnetic rods is that the magnitudes of both the real and imaginary components of the coil impedance, for ferromagnetic rods, are increased in proportion to $\mu_r \gg 1$. Note that the air point, corresponding to the absence of any test-piece, is still found at (0, 1) as in Fig. 6.23 but the scale of the impedance change due to the ferromagnetic test-piece is much larger than for the non-ferromagnetic case for the reasons just mentioned. When the fill factor is reduced, the real and imaginary components of the coil impedance are reduced in direct proportion to the reduction in the fill factor. This means that a change in impedance due to reduction in fill factor cannot be separated from a change due to reduction in test-piece permeability. Fortunately, however, this common direction is usually at a large phase angle compared with changes due to cracks and other longitudinal discontinuities, allowing the latter to be detected. Finally, when the fill factor $\eta = 1$ the intercept of the impedance locus with the vertical axis gives an approximate value for the relative permeability μ_r of the rod.

In a similar manner to the developments presented in Sects. 6.3.3 and 6.3.4, for the circular current filament and the coil above a half-space conductor, electromagnetic analysis of a circular current filament and a coil encircling a solid cylindrical conductor are presented in the following sections. Formulas are developed by

which the value of coil impedance can be calculated using relevant input parameters. Impedance-plane diagrams such as that shown in Fig. 6.23 can be plotted by evaluating the formulas obtained.

6.5.1 *Circular Current Loop Encircling a Solid Cylindrical Conductor*

Governing Equation for E

Consider a filamentary circular current loop, radius a, exterior to a cylindrical conductor with radius ρ_1 and conductivity σ, Fig. 6.25. The conductor in this case is non-ferromagnetic. As in Sect. 6.3.3, the system is axially symmetric so that the current density in the loop is entirely azimuthal, (6.45), immediately implying that the electric field is also purely azimuthal, (6.46). Again, it is assumed that the conductor is linear, isotropic and homogeneous such that constitutive relations (2.25) and (2.33) hold. Formulating the solution in terms of the electric field, (6.48) is obtained as before. Arbitrarily assigning the plane of the current loop to be $z = h$, the following governing equation for the electric field due to a circular current loop coaxial with a circular conductive cylinder is obtained in the quasi-static regime;

$$\left(\frac{\partial^2}{\partial\rho^2} + \frac{1}{\rho}\frac{\partial}{\partial\rho} - \frac{1}{\rho^2} + \frac{\partial^2}{\partial z^2} - k^2\right) E_\phi = j\omega\mu\mathcal{I}\delta(\rho - a)\delta(z - h). \tag{6.98}$$

Solution for E

The solution of (6.98) will be found by the method of separation of variables. Everywhere *off* the current loop, (6.98) may be written

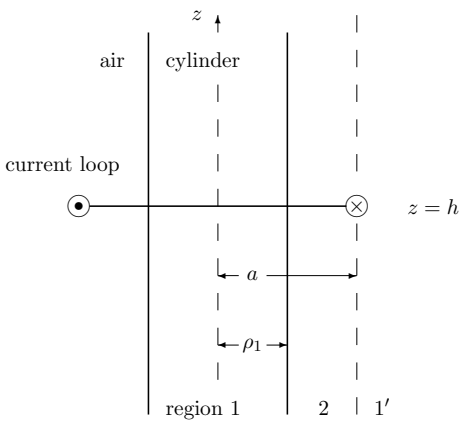

Fig. 6.25 Cross section through the axis of a circular, infinitesimal current loop, coaxial with a solid metal cylinder

$$\left(\frac{\partial^2}{\partial\rho^2}+\frac{1}{\rho}\frac{\partial}{\partial\rho}-\frac{1}{\rho^2}+\frac{\partial^2}{\partial z^2}-k_i^2\right)E_\phi^i=0, \tag{6.99}$$

where $k_i^2=j\omega\mu_i\sigma_i$. The sub- or superscript i may take values 1, 2 and 1′, and refers to regions within the metal cylinder ($\rho<\rho_1$), outside the cylinder but within the current filament ($\rho_1<\rho<a$), and exterior to the current filament ($\rho\geq a$), respectively, as labeled in Fig. 6.25.

Suppose the solution is of the form $E_\phi^i(\rho,z)=R_i(\rho)Z(z)$. The longitudinal part of the solution, $Z(z)$, does not change from one region to another so needs no subscript. (Note that this case is complementary to the case of the planar conductor, Sect. 6.3.3, in which the subscript attaches to the longitudinal part of the solution.) Substitute this form into (6.99) and divide by $R_i(\rho)Z(z)$ to obtain

$$\frac{1}{R_i(\rho)}\frac{\partial^2R_i(\rho)}{\partial\rho^2}+\frac{1}{\rho R_i(\rho)}\frac{\partial R_i(\rho)}{\partial\rho}-\frac{1}{\rho^2}+\frac{1}{Z(z)}\frac{\partial^2Z(z)}{\partial z^2}-k_i^2=0. \tag{6.100}$$

Variables have been separated, i.e., terms in (6.100) depend either on ρ or on z. This means that (6.100) can be separated into two equations by introducing a variable of separation, κ, in the following way:

$$\frac{1}{R_i(\rho)}\frac{\partial^2R_i(\rho)}{\partial\rho^2}+\frac{1}{\rho R_i(\rho)}\frac{\partial R_i(\rho)}{\partial\rho}-\left(\frac{1}{\rho^2}+k_i^2\right)=\kappa^2 \tag{6.101}$$

$$\frac{1}{Z(z)}\frac{\partial^2Z(z)}{\partial z^2}=-\kappa^2. \tag{6.102}$$

The general solution for (6.102) is conveniently written

$$Z(z)=A(\kappa)\sin\kappa(z-h)+B(\kappa)\cos\kappa(z-h)=B(\kappa)\cos\kappa(z-h) \tag{6.103}$$

where $A(\kappa)$ and $B(\kappa)$ are functions of the continuous variable κ. I have immediately put $A(\kappa)=0$ due to the symmetry of the system about the plane of the current filament, $z=h$. The form of $B(\kappa)$ will be determined by other boundary conditions. The differential equation (6.101) governing the radial term has the following general solution,

$$R_i(\rho)=C_i(\kappa)I_1(\gamma_i\rho)+D_i(\kappa)K_1(\gamma_i\rho) \tag{6.104}$$

where $I_1(u)$ and $K_1(u)$ are the modified Bessel functions of the first and second kinds of order 1, respectively (see Sect. 10.4), and $\gamma_i=\sqrt{\kappa^2+k_i^2}$ where the root with positive real part is taken. Note, the sign of κ^2 has been switched in (6.101) and (6.102), compared with (6.52) and (6.53), to preserve the definition of γ_i. One important consequence of this is that the general solution (6.103) is written in terms of the sine and cosine dependence on the spatial variable z, rather than in terms of an exponential dependence on z as in the equivalent general solution for the current loop above a half-space conductor, (6.56). For similar reasons the general solution (6.104)

is written in terms of modified Bessel functions rather than Bessel functions as in (6.54). Since κ is a continuous variable, the electric field is obtained by integrating over the range of κ. Hence, combining (6.103) with (6.104), the general solution of (6.100) may be written

$$E_\phi^i(\rho, z) = R_i(\rho)Z(z) = \int_0^\infty [C_i(\kappa)I_1(\gamma_i\rho) + D_i(\kappa)K_1(\gamma_i\rho)] \cos\kappa(z-h)\, d\kappa, \tag{6.105}$$

where $B(\kappa)$ has been incorporated into $C_i(\kappa)$ and $D_i(\kappa)$. Considering in turn each of the three regions labeled in Fig. 6.25, in region 1—the conductor,

$$E_\phi^1(\rho, z) = \int_0^\infty C_1(\kappa)I_1(\gamma_1\rho) \cos\kappa(z-h)\, d\kappa. \tag{6.106}$$

In region 2, between the current loop and the conductor,

$$E_\phi^2(\rho, z) = \int_0^\infty [C_2(\kappa)I_1(\kappa\rho) + D_2(\kappa)K_1(\kappa\rho)] \cos\kappa(z-h)\, d\kappa, \tag{6.107}$$

and in region $1'$, beyond the current loop,

$$E_\phi^{1'}(\rho, z) = \int_0^\infty D_{1'}(\kappa)K_1(\kappa\rho) \cos\kappa(z-h)\, d\kappa. \tag{6.108}$$

The coefficients are now determined by applying interface conditions between regions 1, 2 and $1'$ in a process analogous to that resulting in (6.60)–(6.63) in Sect. 6.3.3. In particular,

$$E_\phi^1(\rho_1, z) = E_\phi^2(\rho_1, z), \tag{6.109}$$

$$\frac{\partial}{\partial\rho}E_\phi^1(\rho, z)\bigg|_{\rho=\rho_1} = \frac{\partial}{\partial\rho}E_\phi^2(\rho, z)\bigg|_{\rho=\rho_1}, \tag{6.110}$$

$$E_\phi^2(a, z) = E_\phi^{1'}(a, z), \tag{6.111}$$

$$\frac{\partial}{\partial\rho}E_\phi^2(\rho, z)\bigg|_{\rho=a} = \frac{\partial}{\partial\rho}E_\phi^{1'}(\rho, z)\bigg|_{\rho=a} + j\omega\mu\mathcal{I}\delta(z-h). \tag{6.112}$$

Finally, the following expressions for E_ϕ^i are obtained:

$$E_\phi^1(\rho, z) = -\frac{j\omega\mu_0\mathcal{I}a}{\pi}\int_0^\infty K_1(\kappa a)I_1(\gamma_1\rho)\frac{1}{\rho_1^2 D}\cos\kappa(z-h)\, d\kappa, \tag{6.113}$$

$$E_\phi^2(\rho, z) = -\frac{j\omega\mu_0\mathcal{I}a}{\pi}\int_0^\infty K_1(\kappa a)\left\{I_1(\kappa\rho) + \left[\frac{I_1(\gamma_1\rho_1)}{\rho_1^2 D} - I_1(\kappa\rho_1)\right]\frac{K_1(\kappa\rho)}{K_1(\kappa\rho_1)}\right\}\cos\kappa(z-h)\, d\kappa, \tag{6.114}$$

$$E_{\phi}^{1'}(\rho, z) = -\frac{j\omega\mu_0 \mathcal{I} a}{\pi} \int_0^{\infty} K_1(\kappa a) K_1(\kappa\rho) \left\{ \frac{1}{K_1(\kappa\rho_1)} \times \left[\frac{I_1(\gamma_1\rho_1)}{\rho_1^2 D} - I_1(\kappa\rho_1) \right] + \frac{I_1(\kappa a)}{K_1(\kappa a)} \right\} \cos\kappa(z-h)\, d\kappa, \quad (6.115)$$

in which

$$D = \frac{1}{\rho_1} \left[\kappa I_1(\gamma_1\rho_1) K_0(\kappa\rho_1) + \gamma_1 I_0(\gamma_1\rho_1) K_1(\kappa\rho_1) \right]. \quad (6.116)$$

One method for evaluating the integrals in the above equation is mentioned in this text following (6.66).

Calculation of Z

As developed in Sect. 6.3.3 for a current filament above a half-space conductor, the self-induced voltage in the current filament coaxial with a cylindrical rod can be computed by integrating **E**, (6.114) or (6.115), around the current loop. By analogy with (6.68), and dividing by phasor current $\mathcal{I}$ to give impedance, (4.25), the impedance is then obtained by means of

$$Z^{\delta} = -\frac{2\pi a}{\mathcal{I}} E_{\phi}(a, h). \quad (6.117)$$

Inserting $E_{\phi}(a, h)$, determined from either (6.114) or (6.115) into (6.117) yields the self-induced impedance of the current filament, Z^{δ}:

$$Z^{\delta} = 2j\omega\mu_0 a^2 \int_0^{\infty} [K_1(\kappa a)]^2 \left\{ \frac{1}{K_1(\kappa\rho_1)} \left[\frac{I_1(\gamma_1\rho_1)}{\rho_1^2 D} - I_1(\kappa\rho_1) \right] + \frac{I_1(\kappa a)}{K_1(\kappa a)} \right\} d\kappa. \quad (6.118)$$

We see that Z^{δ} depends on the frequency of operation ω, the coil cross-sectional area a^2, its position with reference to the sample, ρ_1, and the sample conductivity σ. The above relation has been derived on the assumption of a non-ferromagnetic test-piece, but if the conductor is in fact ferromagnetic then γ_1 should be replaced by $\gamma_1'/\mu_{r1} = \sqrt{\kappa^2 + j\omega\mu_0\mu_{r1}\sigma_1}/\mu_{r1}$, and Z^{δ} depends also on the relative permeability of the test-piece, μ_{r1}. From relation (6.118) the self-inductance L of the filament can be easily obtained via relation (6.1). Lastly, the impedance of the completely isolated current filament (in the absence of a test-piece), Z_0^{δ}, can be obtained by letting $\sigma_1 \to 0$ in (6.118), i.e., $\gamma_1 \to \kappa$, to obtain

$$Z_0^{\delta} = 2j\omega\mu_0 a^2 \int_0^{\infty} K_1(\kappa a) I_1(\kappa a)\, d\kappa. \quad (6.119)$$

Comparing (6.119) with (6.118) allows us to separate out the contribution to Z^{δ} from the test-piece, as follows.

$$Z^{\delta} = Z_0^{\delta} + 2j\omega\mu_0 a^2 \int_0^{\infty} \frac{[K_1(\kappa a)]^2}{K_1(\kappa\rho_1)} \left[\frac{I_1(\gamma_1\rho_1)}{\rho_1^2 D} - I_1(\kappa\rho_1) \right] d\kappa. \tag{6.120}$$

Lastly, as a point of interest, by comparing result (6.119) with (6.71) it can be deduced that

$$\int_0^{\infty} K_1(x) I_1(x) dx = \frac{\pi}{2} \int_0^{\infty} [J_1(x)]^2 dx.$$

6.5.2 *Coil Encircling a Solid Cylindrical Conductor*

Following a process of superposition, the results for the current loop encircling a solid cylindrical conductor, obtained in the previous section, can be extended to obtain the impedance of a coil with finite cross section, shown in Fig. 6.22. Much of this development is similar to that given in Sect. 6.3.4, for a surface coil with finite cross section positioned above a half-space conductor.

Electric Field

Assuming as before that the current in each loop has the same phase and amplitude, the electric field due to a coil encircling a solid cylindrical conductor can be written, similarly to (6.75);

$$\mathbf{E}^T(\rho, z) = \int_h^{h+l} \int_{r_\mathrm{i}}^{r_\mathrm{o}} \mathbf{E}(\rho, z | a_\mathrm{s}, h_\mathrm{s}) da_\mathrm{s} dh_\mathrm{s} \tag{6.121}$$

wherein a_s and h_s are continuous variables in the radial and vertical directions within the coil cross section.

Voltage in a Coil Encircling a Cylindrical Rod

The total voltage induced in a coil of n turns is given by (6.81) in which $2\pi a_i$ is the circumferential length and h_i is, in this case, the height of the ith current loop above the plane $z = 0$, Fig. 6.22. $E_\phi(a_i, h_i)$ is the electric field of the ith current loop. Replacing the summation by an integral over the cross section of the coil, an equation similar to (6.83) is obtained wherein the notation of Fig. 6.22 is employed:

$$\mathcal{V} = -\frac{2\pi n}{l(r_\mathrm{o} - r_\mathrm{i})} \int_h^{h+l} \int_{r_\mathrm{i}}^{r_\mathrm{o}} a_\mathrm{s} E_\phi(a_\mathrm{s}, h_\mathrm{s}) da_\mathrm{s} dh_\mathrm{s}. \tag{6.122}$$

Z for a Coil Encircling a Cylindrical Rod

Following a development similar to that for (6.84), the following equation for impedance of a coil encircling a cylindrical rod is obtained:

$$Z = -\frac{2\pi n^2}{l^2(r_\mathrm{o} - r_\mathrm{i})^2} \int_h^{h+l} \int_{r_\mathrm{i}}^{r_\mathrm{o}} a_\mathrm{s} E_\phi(a_\mathrm{s}, h_\mathrm{s}) da_\mathrm{s} dh_\mathrm{s}. \tag{6.123}$$

Now the integrals with respect to a_s and h_s may be evaluated by inserting $E_\phi(a_s, h_s)$ into (6.123). To do this, the integral over a_s is divided into two, covering coil regions within and beyond a_s. In the region within a_s the expression for $E_\phi^2(\rho, z)$ is inserted whereas in the region beyond a_s the expression for $E_\phi^{1'}(\rho, z)$ is used. Explicitly,

$$Z = -\frac{2\pi n^2}{l^2(r_o - r_i)^2} \int_h^{h+l} \left[\int_{r_i}^{a_s} a_s E_\phi^2(a_s, h_s) da_s + \int_{a_s}^{r_o} a_s E_\phi^{1'}(a_s, h_s) da_s \right] dh_s. \tag{6.124}$$

Inserting expressions for $E_\phi^2(\rho, z)$ and $E_\phi^{1'}(\rho, z)$ into (6.124) and changing the order of integration, the following integrals with respect to a_s and h_s emerge:

$$Z = \frac{2j\omega\mu_0 n^2}{l^2(r_o - r_i)^2} \int_0^\infty \int_h^{h+l} \int_{r_i}^{r_o} a_s^2 \{K_1(\kappa a_s) I_1(\kappa a_s) + \frac{[K_1(\kappa a_s)]^2}{K_1(\kappa \rho_1)} \left[\frac{I_1(\gamma_1 \rho_1)}{\rho_1^2 D} - I_1(\kappa \rho_1) \right] \right\} \cos \kappa (h_s - h)\, da_s dh_s d\kappa, \tag{6.125}$$

assuming that the current in each loop has the same phase and amplitude. Integration with respect to h_s is straightforward and yields the following.

$$Z = \frac{2j\omega\mu_0 n^2}{l^2(r_o - r_i)^2} \int_0^\infty \int_{r_i}^{r_o} \frac{a_s^2}{\kappa} \{K_1(\kappa a_s) I_1(\kappa a_s) + \frac{[K_1(\kappa a_s)]^2}{K_1(\kappa \rho_1)} \left[\frac{I_1(\gamma_1 \rho_1)}{\rho_1^2 D} - I_1(\kappa \rho_1) \right] \right\} \sin \kappa l\, da_s d\kappa. \tag{6.126}$$

Recognizing that (6.126) can be written as the sum of the impedance of the isolated coil, Z_0, and a term representing the effect of the conductor, the following is obtained.

$$Z = Z_0 + \frac{2j\omega\mu_0 n^2}{l^2(r_o - r_i)^2} \int_0^\infty \int_{r_i}^{r_o} \frac{a_s^2}{\kappa} \frac{[K_1(\kappa a_s)]^2}{K_1(\kappa \rho_1)} \left[\frac{I_1(\gamma_1 \rho_1)}{\rho_1^2 D} - I_1(\kappa \rho_1) \right] \sin \kappa l\, da_s d\kappa, \tag{6.127}$$

where

$$Z_0 = \frac{2j\omega\mu_0 n^2}{l^2(r_o - r_i)^2} \int_0^\infty \int_{r_i}^{r_o} \frac{a_s^2}{\kappa} K_1(\kappa a_s) I_1(\kappa a_s) \sin \kappa l\, da_s d\kappa. \tag{6.128}$$

Finally, the expression for Z can be simplified by expressing the integral with respect to a_s as follows.

$$\int_{r_i}^{r_o} [a_s K_1(\kappa a_s)]^2 da_s = \frac{1}{\kappa^4} K^2(\kappa r_i, \kappa r_o) \tag{6.129}$$

where

$$K^2(x_1, x_2) = \int_{x_1}^{x_2} [x K_1(x)]^2 dx. \tag{6.130}$$

This integral must be evaluated numerically but allows us to write the following expression for the impedance of a coil of finite cross section coaxial with and encircling a solid cylindrical conductor.

$$Z = Z_0 + \frac{2j\omega\mu_0 n^2}{l^2(r_o - r_i)^2} \int_0^\infty \frac{K^2(\kappa r_i, \kappa r_o)}{\kappa^5} \frac{1}{K_1(\kappa\rho_1)} \left[\frac{I_1(\gamma_1\rho_1)}{\rho_1^2 D} - I_1(\kappa\rho_1) \right] \sin \kappa l \, d\kappa. \tag{6.131}$$

As already noted in Sect. 6.3.4, Z depends on the probe's frequency of operation, ω, the coil dimensions, r_i, r_o and l, the square of the number of turns, n^2, the coil position with reference to the sample—here specified by r_i and r_o, and the sample conductivity, σ. Evaluation of (6.131) for particular coil and sample parameters allows impedance-plane diagrams such as that shown in Fig. 6.23 to be developed. The frequency-dependent curves shown in Fig. 6.23 are obtained by varying ω and the fill factor-dependent curves by varying r_i or ρ_1 in (6.131).

6.5.3 Sources of Uncertainty

In a system of cylindrical symmetry, such as a coil encircling a cylindrical conductor, two sources of geometrical uncertainty exist; coil tilt and wobble. Tilt occurs when the coil axis tilts through a finite angle with respect to the axis of the test-piece and has been analyzed in detail by Theodoulidis and Skarlatos [18]. Wobble occurs when the coil axis is laterally displaced from the axis of the test-piece and has been analyzed by Theodoulidis [19] in the case of a bobbin coil (Sect. 6.6.1).

6.6 Bobbin Coil

Bobbin coils offer effective coupling with the interior of tube-like specimens. A bobbin coil is oriented with its axis parallel to the axis of the cylindrical cavity (e.g., a tube interior or a bore hole) in a test-piece and is designed to be threaded through it. Bobbin probes are very commonly used in differential mode for optimum defect detection, as discussed in Sect. 8.3. One application in which bobbin probes are commonly used is in the inspection of nuclear power plant steam generator tubes. Threading a bobbin probe through a tube offers shorter inspection time than using a rotating surface probe, which is common in borehole inspection, Fig. 6.5. A schematic diagram of a bobbin coil coaxial with a borehole is shown in Fig. 6.26.

In a definition analogous to that given in (6.97) for the encircling coil geometry, the fill factor of the bobbin coil, η_b, is defined as follows, with reference to the notation of Fig. 6.26.

$$\eta_b = \left(\frac{r_o}{\rho_1} \right)^2. \tag{6.132}$$

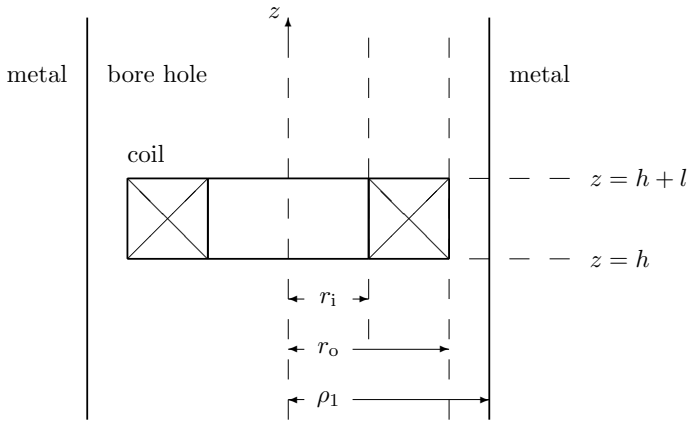

Fig. 6.26 Cross section through the axis of a circular bobbin coil coaxial with the bore of the test-piece

Since the bobbin coil is primarily applied in tube inspection, rather than in borehole inspection, a detailed discussion of the impedance calculation for the bobbin coil is deferred to Sect. 7.2.6 where test-pieces with more than one interface (in this case the interior and exterior surfaces of the tube) are considered. Example impedance-plane plots for a bobbin coil internal to a tube are given in Fig. 7.6 for a tube with fixed ratio of wall thickness to outer diameter, and in Fig. 7.7 for a bobbin coil internal to a tube with varying ratio of wall thickness to outer diameter. The curves plotted in those figures are also applicable to coils encircling tube-like test samples.

6.6.1 Sources of Uncertainty

For the configuration of a bobbin probe inserted into a tube or a borehole, a source of noise in the measurement may be probe "wobble". This is a type of geometrical noise, caused by the movement of the probe. Ideally, the coil is coaxial with the tube, but wobble of the probe may cause the coil axis to shift a finite distance from the tube axis, as shown in Fig. 6.27. Some of the effects of probe wobble on the impedance-plane plot are shown in Fig. 6.28, at three distinct frequencies. For comparison, the effects of 10% inner diameter (ID) or outer diameter (OD) wall thinning of the tubular test-piece are also shown. Noting that the "f_{90}" frequency is defined as the frequency that provides approximately 90° phase separation between shallow ID and OD defects, the three frequencies for which comparisons are plotted in Fig. 6.28 are $f_{90}/2$, f_{90} and $2f_{90}$. The frequency f_{90} and may be computed using the empirical expression

$$f_{90} = \frac{516\sigma}{T^2} \tag{6.133}$$

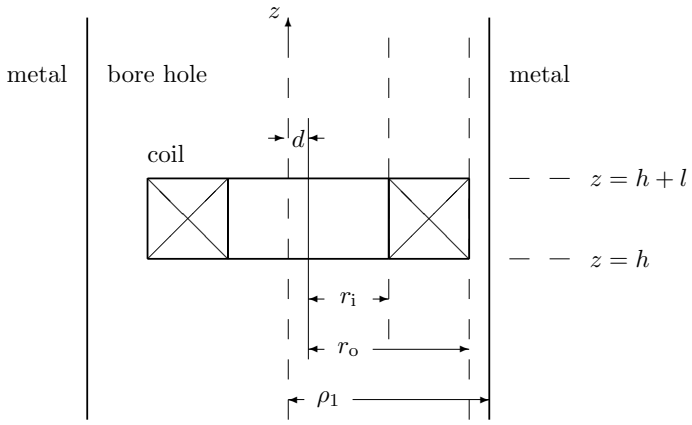

Fig. 6.27 Cross section through the axis of a circular bobbin coil that is offset by distance d from the axis of the test-piece bore

where σ is in %IACS, T is the tube wall thickness in mm and the result is in kHz.

Also shown in Fig. 6.28 is the sum of the ID and OD signals with the signal due to wobble at maximum axis offset. It can be seen that the phase angle between ID and OD thinning increases as frequency increases and that the amplitude of the OD signal decreases with increasing frequency due to the skin effect. For OD wall thinning the deleterious effect of wobble on the flaw signal can be seen clearly at frequency $2\,f_{90}$, for which the signal due to probe wobble overwhelms that due to the flaw.

6.7 Summary

This chapter has dealt with classical solutions to canonical problems in the theory of eddy-current nondestructive evaluation and has examined sources of uncertainty in EC NDE. The impedance of an EC coil was expressed for test-pieces with half-space (Cartesian) and rod or borehole (cylindrical) geometries. Upon this foundation, the effect of introducing additional boundaries to the test-piece is considered in Chap. 7. Following this approach, the EC inspection of plates, tubes, surface coatings or material under surface coatings can be modeled. A method for modeling the effect of test-piece edges on the EC signal is also introduced. The ability to model the effect of such geometrical features on the EC signal provides a pathway for separating such effects from a flaw signal.

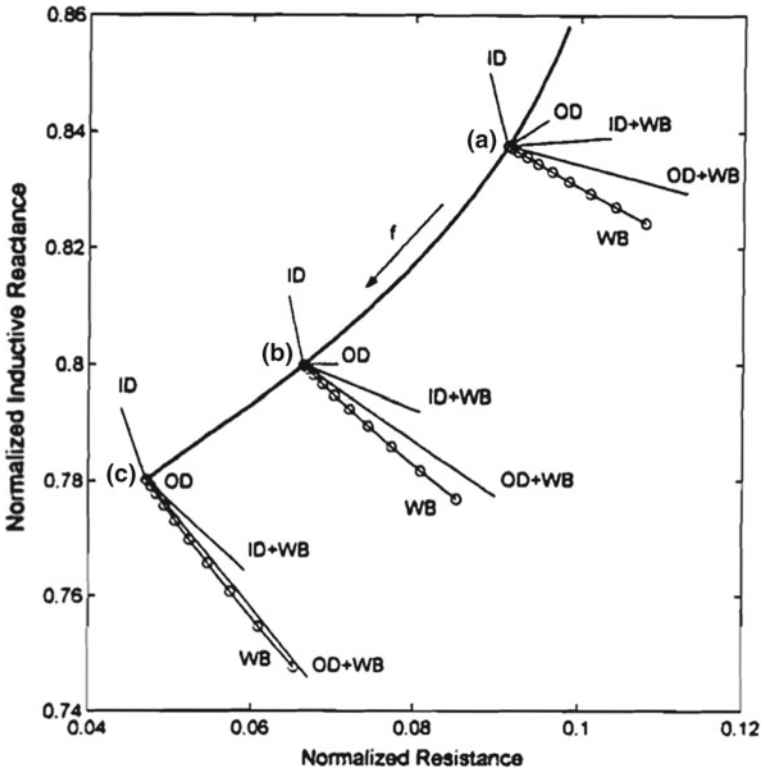

Fig. 6.28 ΔZ due to 10% inner diameter (ID) and 10% outer diameter (OD) uniform thinning, wobble (WB), and their superposition for maximum offset, at three frequencies: **a** $f_{90}/2$, f_{90} and $2f_{90}$ [19]. With kind permission from Springer Science and Business Media: *Res. Nondestruct. Eval.*, vol. 4, 2002, p. 120, Analytical modeling of wobble in eddy-current tube testing with bobbin coils, T. P. Theodoulidis, Fig. 2. Original caption: Impedance changes due to 10%ID and 10%OD uniform thinning, wobble, and their superposition for maximum offset, at three frequencies: **(a)** $f_{90}/2$; **(b)** f_{90}; **(c)** $2f_{90}$

6.8 Exercises

1. Show that the magnetic field in a region of space that contains a phasor current source $\mathbf{J}_s$ (varying as the real part of $e^{j\omega t}$) and a conductor carrying induced eddy-current density $\mathbf{J}_{ec} = \sigma\mathbf{E}$, where σ is the conductivity of the metal, obeys the following governing equation

$$\left(\nabla^2 - j\omega\mu\sigma\right)\mathbf{H} = -\nabla \times \mathbf{J}_s.$$

Hint: Follow a method similar to that used to determine (6.10), but now begin by taking the curl of (6.6) rather than of (6.5).

2. Apply the Biot–Savart Law to obtain the following expression for B_z along the axis of a circular current loop with radius a carrying current I, whose axis coincides with that of a cylindrical coordinate system.

$$B_z = \frac{\mu_0 I}{2} \frac{a^2}{(a^2 + z^2)^{3/2}} \tag{6.134}$$

3. A long solenoid consists of n similar loops of wire, per unit length, each with radius a. The axis of the solenoid coincides with the z-axis of a cylindrical co-ordinate system. The magnetic field inside the solenoid is uniform over its cross-sectional area and is given by

$$H_z = nI, \tag{6.135}$$

where I is the magnitude of the current flowing in the wire. Show that the inductance per unit length of a solenoid filled with a ferromagnet whose permeability is μ is given by

$$L = \mu\pi(na)^2 \tag{6.136}$$

and that the normalized impedance of the coil per unit length is given by

$$\frac{Z}{X_0} = \frac{R_0}{\omega\mu_0\pi(na)^2} + j\mu_r \tag{6.137}$$

where R_0 is the DC resistance of the coil. Plot Z/X_0 on an impedance-plane plot.

4. Take the curl of the vector potential given in (6.36) to obtain the expressions for B_r and B_z given in (6.42) and (6.43).[1] Show that, on the axis, the result for B_z of (6.43) reduces to that obtained by the Biot–Savart Law, Exercise 2.
5. We know from interface conditions (Sect. 5.6) that the tangential component of the electric field must be continuous at a boundary. Show that $E_\phi(r, z)$ for the filamentary coil above a half-space conductor in (6.64)–(6.66) is continuous at $z = h$ and $z = 0$.
6. Suppose the conductive half-space interrogated by a filamentary current loop, as in Sect. 6.3.3, now has a surface layer with depth d and conductivity σ_3 (region 3, $-d \le z \le 0$). The substrate conductivity is now σ_4 (region 4, $z \le -d$). Hence $\gamma_i = \sqrt{\kappa^2 + j\omega\mu_0\sigma_i}$ with $i = 3, 4$. In this case,

[1] Hint: In definitions (6.37) and (6.38), k is known as the *modulus* of these integrals. The following functional relations between elliptic integrals are given in Eqs. 8.123.2 and 8.123.4 of [20].

$$\frac{dK(k)}{dk} = \frac{E(k)}{kk'^2} - \frac{K(k)}{k}$$
$$\frac{dE(k)}{dk} = \frac{E(k) - K(k)}{k}$$

In these relations, k' is known as the complementary modulus and $k' = \sqrt{1 - k^2}$; $k^2 < 1$.

$$E_{\phi}^{1}(\rho,z) = -\frac{1}{2}j\omega\mu_0 Ia\int_0^{\infty} J_1(\kappa a)J_1(\kappa r)e^{-\kappa(h+z)} \times\left\{e^{2\kappa h}+\frac{(\kappa+\gamma_3)(\gamma_3-\gamma_4)+(\kappa-\gamma_3)(\gamma_3+\gamma_4)e^{2\gamma_3 d}}{(\kappa-\gamma_3)(\gamma_3-\gamma_4)+(\kappa+\gamma_3)(\gamma_3+\gamma_4)e^{2\gamma_3 d}}\right\}d\kappa. \tag{6.138}$$

Identify two limits in which this result should reduce to the result for the half-space conductor and show that (6.138) does indeed reduce to (6.64) in these limits.

7. Show how the factor μ_r appears in relation (6.70), in the case of a ferromagnetic test-piece.

References

1. Hugo, G.R.: Impedance changes in a coil due to a nearby small conducting sphere. J. Phys. D: Appl. Phys. **21**, 33–38 (1988)
2. Kolyshkin, A.A., Vaillancourt, R.: Impedance of a single-turn coil due to a double-layered sphere with varying properties. IEEE T. Magn. **31**, 2274–2280 (1995)
3. Theodoulidis, T.P., Kriezis, E.E.: Coil impedance due to a sphere of arbitrary radial conductivity and permeability profiles. IEEE T. Magn. **38**, 1452–1460 (2002)
4. Moore, P.O. (ed.), Udpa, S.S. (tech. ed.): Nondestructive Testing Handbook: Electromagnetic Testing, vol. 5, 3rd edn. American Society for Nondestructive Testing, Columbus (2004)
5. Badics, Z., Matsumoto, Y., Aoki, K., Nakayasu, F., Kurokawa, A.: Finite element models of stress corrosion cracks (SCC) in 3-D eddy current NDE problems. In: Collins, R., Dover, W.D., Bowler, J.R., Miya, K. (eds.) Nondestructive Testing of Materials. Studies in Applied Electromagnetics and Mechanics, vol. 8, pp. 21–30. IOS Press, Amsterdam (1995)
6. Grimberg, R., Savin, A., Radu, E., Mihalache, O.: Nondestructive evaluation of the severity of discontinuities in flat conductive materials by an eddy-current transducer with orthogonal coils. IEEE T. Magn. **36**, 299–307 (2000)
7. Van Bladel, J.: Electromagnetic Fields. Hemisphere Publishing Corporation, Washington (1985)
8. Dodd, C.V., Deeds, W.E.: Analytical solutions to eddy-current probe-coil problems. J. Appl. Phys. **39**, 2829–2838 (1968)
9. Dodd, C.V., Cheng, C.C., Deeds, W.E.: Induction coils coaxial with an arbitrary number of cylindrical conductors. J. Appl. Phys. **45**, 638–647 (1974)
10. Theodoulidis, T.P., Kriezis, E.E.: Eddy Current Canonical Problems (with Applications to Nondestructive Evaluation). Tech Science Press, Forsyth (2006)
11. Ferroxcube product web pages
12. Theodoulidis, T.P.: Model of ferrite-cored probes for eddy current nondestructive evaluation. J. Appl. Phys. **93**, 3071–3078 (2003)
13. Lu, Y., Bowler, J.R., Theodoulidis, T.P.: An analytical model of a ferrite-cored inductor used as an eddy current probe. J. Appl. Phys. **111**, 103907 (2012)
14. Harrison, D.J., Jones, L.D., Burke, S.K.: Benchmark problems for defect size and shape determination in eddy-current nondestructive evaluation. J. Nondestruct. Eval. **15**, 21–34 (1996)
15. Bowler, N., Huang, Y.: Electrical conductivity measurement of metal plates using broadband eddy-current and four-point methods. Meas. Sci. Technol. **16**, 2193–2200 (2005)
16. Theodoulidis, T.P.: Analytical model for tilted coils in eddy current nondestructive evaluation. IEEE T. Magn. **41**, 2447–2454 (2005)

17. McMaster, R.C., McIntire, P. (eds.), Mester, L.M. (tech. ed.): Nondestructive Testing Handbook: Electromagnetic Testing, vol. 4, 2nd edn. American Society for Nondestructive Testing, Columbus (1986)
18. Theodoulidis, T.P., Skarlatos, A.: Eddy current interaction of an arbitrarily positioned probe coil with a conductive cylinder. IEEE T. Magn. **48**, 2392–2394 (2012)
19. Theodoulidis, T.P.: Analytical modeling of wobble in eddy current tube testing with bobbin coils. Res. Nondestruct. Eval. **14**, 111–126 (2002)
20. Gradshteyn, I.S., Ryzhik, I.M. (eds.): Table of Integrals, Series and Products, 6th edn. Academic, London (2000)